

Radboud Universiteit



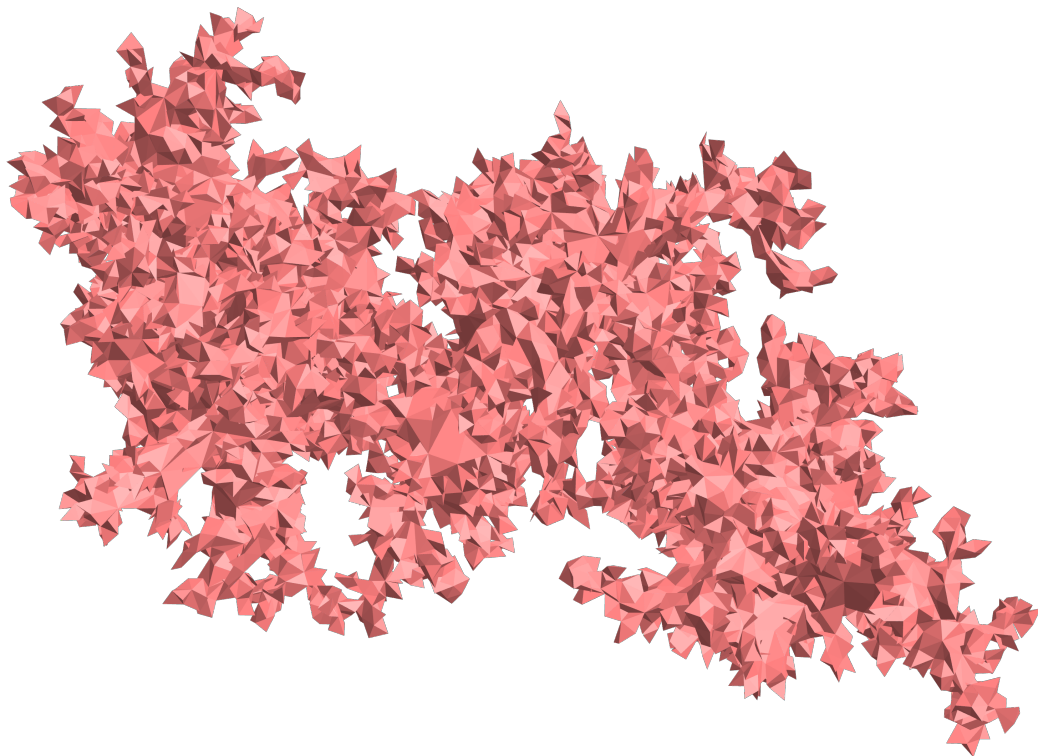
MASTER THESIS

Curvature in 2D Euclidean quantum gravity

Thijs Niestadt

Supervisor:
prof. Renate Loll

Second reader:
prof. Jan Ambjørn



January 29, 2024

Abstract

A numerical study of curvature in quantum gravity is presented. Specifically, the quantum Ricci curvature is studied in two-dimensional Euclidean dynamical triangulations (2D EDT), using Monte Carlo simulations. Recent measurements suggested that the curvature properties of 2D EDT are best approximated by those of a *five*-sphere. The present work aims to improve upon this analysis, by eliminating finite-size effects. In addition to the usual combinatorial triangulations, the measurements are also performed on two ensembles of degenerate triangulations, which are part of the same universality class. We find that the curvature properties of 2D EDT are best approximated by those of a *four*-sphere. Additionally, measurements of the Hausdorff dimension are performed for the three ensembles.

Contents

1	Introduction	1
2	Theoretical background	3
2.1	From classical to quantum gravity	3
2.2	Discretization in 2D	4
2.2.1	Combinatorial manifolds	4
2.2.2	Applying gravitational action to triangulations	6
2.2.3	Continuum limit and universality	8
2.3	Triangulation Ensembles	8
2.3.1	Restricted degenerate ensemble	9
2.3.2	Maximally degenerate ensemble	10
2.4	Observables	11
2.4.1	Quantum Ricci Curvature	11
2.5	Sampling triangulations	14
3	Monte Carlo practicalities	16
3.1	Initialization	16
3.2	Equilibration	17
3.3	Autocorrelation	18
4	Hausdorff Dimension	22
4.1	Methods	22
4.2	Results	23
4.3	Discussion	25
5	Average Sphere Distance	28
5.1	Methods	28
5.2	Results for combinatorial triangulations	29
5.3	Results for degenerate triangulations	30
5.4	Discussion	31
5.4.1	Discrepancy with previous work	31
5.4.2	Discretization effects	33
5.4.3	Finite-size effects	34
5.5	Summary of incremental improvements	36
6	Conclusion	38
A	Link and vertex picture equivalence	39
B	Vertex links in the degenerate ensembles	42
C	Average sphere distance on a hypersphere	47
D	Edge flip ergodicity	50
	Bibliography	54

Chapter 1

Introduction

General relativity has been successful in describing gravity at large scales. It has provided verified predictions of planetary orbits [1], black holes [2], and gravitational waves [3, 4]. However, there are strong indications that it cannot be the whole story. A prevalent feature of general relativity is the occurrence of singularities in its solutions, like at the centers of black holes or the big bang. A theory of quantum gravity is expected to allow us to understand the physics at these short length scales. The length scale at which such a theory must certainly be taken into account is given by the Planck length

$$l_p = \sqrt{\frac{\hbar G_N}{c^3}} \approx 1.616 \times 10^{-35} \text{m}, \quad (1.1)$$

with \hbar being the (reduced) Planck constant, G_N Newton's constant, and c the speed of light. The corresponding energy scale is far out of reach for any experimental setup currently available. Of course, the effects of quantum gravity may still be felt at lower energy scales, but nonetheless experimental and observational guidance for how to construct a theory of quantum gravity is not available presently.

A plethora of candidates for a theory of quantum gravity have been proposed. In order to make progress in this discussion, extraction of results from these candidates is needed. Obtaining predictions for physical observables makes it possible to compare the different approaches to quantum gravity, and is crucial for eventual verification through experiment.

A central quantity in General Relativity is curvature. In the classical situation, information about curvature is captured in the Riemann tensor, and is straightforward to compute from the metric tensor $g_{\mu\nu}$ and its derivatives. However, in a nonperturbative quantum gravity setting the derivatives of $g_{\mu\nu}$ may not be available, and as a consequence it is not clear how to go about measuring curvature. Recently, a prescription for defining curvature called *Quantum Ricci Curvature* (QRC) was introduced[5]. A key feature of this quantity is that it does not rely on tensor calculus, but instead relies on distances and volumes. This property makes it particularly suitable for application to (Causal) Dynamical Triangulations. In this setting the gravitational path integral is defined as the continuum limit of a sum over piecewise flat manifolds. Due to their non-smoothness, these manifolds provide a good example of a case where the classical approach to curvature is not applicable, and a prescription like the QRC is useful.[6]

Quantum Ricci Curvature measurements have been performed on a variety of spaces. Namely, on constantly curved smooth spaces and well-behaved lattices [5], on 2D Euclidean Dynamical Triangulations (2D EDT) [7], and on 2D CDT [8]. Additionally, two-point functions based on QRC are being studied [9]. A rather striking conclusion was drawn from the 2D EDT measurements. The QRC measurements on the quantum geometry were compared to that of a D -sphere, for $D = 2, \dots, 5$. It was concluded that the constantly curved space best approximating the curvature in 2D Euclidean quantum gravity is the 5-sphere. While there is no analytic prediction for this dimension, 5 is at odds with other notions of dimension that are known for this geometry, namely, its topological dimension of 2, the Hausdorff dimension $d_H = 4$ [10, 11], and the spectral dimension $d_s = 2$ [12]. This disagreement warrants a further investigation.

In this work, a refinement of the previous work concerning curvature in 2D EDT is presented. Improvements to the fitting procedure are implemented. Furthermore, three triangulation classes, or ensembles, with the same continuum limit are studied numerically using Monte Carlo methods. It turns out that the different triangulation classes provide an additional tool in helping to distinguish discretization effects from physically relevant results. Gaining understanding of the influence of the choice of ensemble on the evaluation of quantum gravity observables also has intrinsic value. For example, it may reveal whether

a specific choice of ensemble causes the continuum limit to be reached faster.

Chapter 2 provides the necessary theoretical background on the following: quantum gravity, and in particular 2D EDT, is introduced. Furthermore, the different triangulation ensembles are defined, as well as the average sphere distance, from which the QRC is obtained. Finally, the algorithm for sampling triangulations is presented. The practical considerations that come with the Markov chain Monte Carlo method are presented in chapter 3. Measurements, along with a discussion, of the Hausdorff dimension and average sphere distance are given in chapters 4 and 5 respectively. Finally, a conclusion and suggestions for further research are given in chapter 6.

Chapter 2

Theoretical background

2.1 From classical to quantum gravity

In general relativity, gravity is a consequence of spacetime curvature. Light and matter follow geodesics in this spacetime, and the curvature is a consequence of its matter (and energy) contents. The metric properties of spacetime are encoded in the Lorentzian metric $g_{\mu\nu}$. Given the matter and energy contents in the form of the stress-energy tensor $T_{\mu\nu}$, the equations of motion for $g_{\mu\nu}$, the Einstein equations, are given by,

$$R_{\mu\nu} - \frac{1}{2}Rg_{\mu\nu} = \kappa T_{\mu\nu} - \Lambda g_{\mu\nu}, \quad (2.1)$$

where $R_{\mu\nu}$ is the Ricci tensor, $R = g^{\mu\nu}R_{\mu\nu}$ the Ricci scalar, and Λ the cosmological constant. The constant κ relates to Newton's gravitational constant G_N as $\kappa = \frac{8\pi G_N}{c^4}$. Interpreting the cosmological constant term as a vacuum energy, one can interpret equation (2.1) as follows; curvature, the left-hand side, is generated by the universe's matter content, the right-hand side. These equations of motion can be obtained using the principle of least action. The action needed is the following:

$$S = \frac{1}{2\kappa} \int d^4x \sqrt{|g|} (R - 2\Lambda) + \int d^4x \sqrt{|g|} \mathcal{L}_M. \quad (2.2)$$

Here, g denotes the determinant of the metric, such that $\int d^4x \sqrt{|g|}$ is a spacetime volume integral. Furthermore, \mathcal{L}_M is the matter Lagrangian. The first part of (2.2), without matter, will from now on be referred to as the Einstein-Hilbert action S^{EH} .

A non-perturbative quantum theory of gravity is obtained using the Feynman path integral formalism [13]. The quantity of interest is the gravitational path integral,

$$Z = \int \mathcal{D}[g_{\mu\nu}] e^{iS^{EH}[g_{\mu\nu}]}. \quad (2.3)$$

Note the usage of natural units, i.e., $\hbar = c = 1$. Furthermore, the integral is over equivalence classes of Lorentzian metrics under diffeomorphisms, $[g_{\mu\nu}]$. This can be understood as follows. The physics is determined by the geometry of spacetime, and metrics related to each other by a spacetime diffeomorphism describe the same geometry. In the path integral, one assigns a phase factor to each physically inequivalent configuration. It is therefore necessary to integrate over geometries, and these are uniquely captured by diffeomorphism equivalence classes of the metric. Stating this prescription for the configuration space is easy, working with it is not. In fact, the path integral stated above is ill-defined for a host of reasons. For a brief overview, see [14], and specifically question 24 therein. A key feature is that the complex nature of the path integral of eq. (2.3) poses difficulties when employing numerical methods. The usual quantum field theory approach to this problem is by using a Wick rotation. While that works well in a fixed Minkowski background, there is no Wick rotation for general smooth metrics.

To sidestep this problem, a different theory is often considered, namely that of Euclidean quantum gravity. While there is no obvious way to relate its results to the Lorentzian theory, the path integral of the Euclidean theory has the computational advantage of being a real quantity. It is given by

$$Z_{EU} = \int \mathcal{D}[g_{\mu\nu}^{EU}] e^{-S^{EH}[g_{\mu\nu}^{EU}]}, \quad (2.4)$$

with

$$S^{EH}[g_{\mu\nu}^{EU}] = \frac{1}{2\kappa} \int d^4x \sqrt{g}(-R + 2\Lambda). \quad (2.5)$$

Now, $[g_{\mu\nu}^{EU}]$ denotes a diffeomorphism equivalence class of Euclidean metrics, in contrast to the Lorentzian ones of before. As can be seen, all constituents of this path integral are now real, making it much more suitable for numerical approaches. However, other problems still persist. The action is not quadratic in the metric $g_{\mu\nu}^{EU}$ and consequently, the functional integral is not Gaussian. Furthermore, the action is not bounded from below. A possible approach of making sense of this path integral nonperturbatively is to define it as a continuum limit of a sum over piecewise flat geometries. The details of such a discretization are presented in section 2.2. In this thesis, a 2D variant of the Euclidean theory is considered. The treatment will focus on the two-dimensional theory, unless specified otherwise.

2.2 Discretization in 2D

As mentioned at the end of section 2.1, the two-dimensional path integral can be solved by viewing it as a continuum limit of a sum over piecewise flat geometries. To this end, a suitable discretization is chosen. The approach of studying a quantum theory in non-perturbative way by discretization is historically well-motivated. The non-perturbative regime of quantum chromodynamics (QCD) has been successfully studied by putting in on a lattice [15]. This method cannot be directly copied to the quantum gravity path integral. In lattice QCD, the dynamical fields are put on the edges between discrete points of space. In contrast, in quantum gravity the geometry of space *is* the dynamical field. Consequently, there exists no obvious background to put it on.

An approach used to discretize the *classical* theory of gravity is that of Regge calculus [16, 17]. The smooth solutions to equation (2.1) are approximated by piecewise flat ones: a “gluing” of simplices, or triangulation. An approximate solution is obtained by varying the edge lengths such that the action is extremized. The details of how one evaluates the gravitational action on a piecewise flat geometry, and particularly how one assigns curvature in the case of equilateral triangulations, is presented in section 2.2.2. An important feature of this discretization is the absence of a need for coordinates. The redundant degrees of freedom that originate from the choice of coordinates are eliminated.

In the theory of Dynamical Triangulations (DT) the path integral is performed by considering triangulations of equilateral simplices. The action is evaluated using the Regge calculus prescription. The edge length a serves as a cut-off scale. By fixing the edge length, the geometry is completely specified by the simplex connectivity. The path integral over equivalence classes of metrics now becomes a sum over inequivalent abstract triangulations. Which triangulations are exactly included in this summation still needs to be addressed. There exists no clear best choice a priori. In 2D, a common choice is that of combinatorial manifolds, the details of which are presented in section 2.2.1. Two alternative classes of triangulations are presented in section 2.3. It should be noted that these three are by no means an exhaustive list of the possible discretization schemes that can be successfully used. The continuum limit of the theory can be obtained using a variety of different, discrete ingredients: the theory exhibits universality. A more detailed discussion of the continuum limit is presented in section 2.2.3.

2.2.1 Combinatorial manifolds

A complete treatment of combinatorial manifolds is outside the scope of the present work. Fortunately, the 2D case lends itself well to a more basic introduction, which will be the approach taken in this section. Consequently, the following is not an exhaustive treatment of the subject. Unless mentioned otherwise, the treatment only considers combinatorial manifolds without boundaries, and of spherical topology. For a complete and well-illustrated treatment of combinatorial manifolds, see chapter 10 of [18].

Let us begin with the definition of a simplex. Given points x_0, \dots, x_n in \mathbb{R}^m , the simplex σ is defined as the convex hull of these points, i.e., all points x for which holds

$$x = \sum_{i=0}^n \lambda_i x_i, \quad (2.6)$$

where $\sum_{i=0}^n \lambda_i = 1$, and $\lambda_i \geq 0$. The dimension of σ is n ; the points x_i are the vertices of σ . A face of σ is a simplex defined by a subset of the vertices of σ . If a face is a simplex of dimension $n - 1$, it is called a facet. Simplices of dimensions 0, 1, 2 are called vertices, edges, and triangles, respectively.

By gluing simplices of dimension d , one can make a simplicial complex of dimension d^1 . This requires that the simplices are glued “nicely”: the intersection of two simplices is either empty, or a face of both simplices. In 2D, this means that the intersection of two triangles is either empty, a vertex, or an edge.

The star st of a simplex σ is the union of all simplices that have σ as a face. The link lk of a simplex σ is the union of the simplices τ in $st(\sigma)$ with $\tau \cap \sigma = \emptyset$. An example showing the star and link of a vertex is shown in Fig. 2.1.

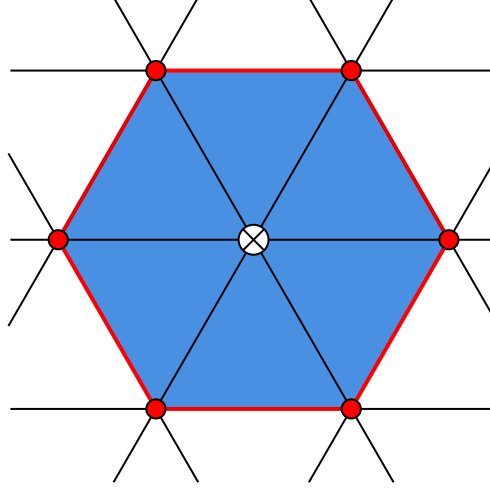


Figure 2.1: Example of the link (in red) and star (in blue) of a vertex (marked with a cross).

Let us now restrict ourselves to complexes built by gluing triangles, and only consider the case of no boundaries, i.e., no edge is left unglued. The dimension d of such a complex is 2. A face σ of dimension n of a d -dimensional complex is *nonsingular* if its link satisfies

$$lk(\sigma) \cong S^{d-n-1}, \quad (2.7)$$

given $n \leq d - 1$, and where S^d is the unit d -sphere.

These definitions finally allow for the definition of a combinatorial manifold. A simplicial complex is a combinatorial manifold if every vertex and edge is nonsingular. That means that for a combinatorial 2-manifold, the link of every vertex is homeomorphic to the unit 1-sphere and the link of every edge is homeomorphic to the 0-sphere: it consists of two distinct vertices. This method of defining combinatorial manifolds is from now on referred to as the *link picture*. The absence of nonsingular edges, together with the aforementioned restriction of nice gluings, it follows that triangles are always glued pairwise along edges, e.g., exactly two triangles meet at every edge.

Alternative definitions and their equivalence

In literature related to Dynamical Triangulations, combinatorial manifolds are often presented under different names, and with differently worded definitions. For example, they may be called simplicial manifolds [19], or combinatorial triangulations [20]. In [20], the author also provides a different definition: A pairwise gluing of triangles without boundary is a combinatorial triangulation if:

1. The vertices of any simplex are distinct from each other, and
2. each edge and triangle is uniquely defined by the list of its vertices.

This method of defining combinatorial manifolds is from now on referred to as the *vertex picture*. It can be shown that this prescription is equivalent to the link picture. The equivalence of these prescriptions is presented in appendix A.

Furthermore, this class of triangulations is often specified by stating restrictions on the dual graph. The dual graph is obtained by placing a vertex on the interior of every triangle, and connecting these

¹Note that the distinction of a simplicial complex and its geometric realization has been omitted from the present treatment. This distinction is also absent from the definitions of the star and link later on. For the current discussion, this distinction is not needed. However, note that this shortcut does lead to some slight abuse of the terminology used in [18].

whenever their corresponding triangles share an edge. Consequently, vertices of degree q in the triangulation become faces with q sides in the dual graph. For triangulations, the dual graphs are ϕ^3 diagrams. Specifically, the dual graphs of triangulations of spherical topology are planar ϕ^3 diagrams without external lines. Combinatorial triangulations are those triangulations that have no self-energies or tadpoles in their dual graph. This way of defining combinatorial manifolds is from now on referred to as the *dual graph picture*.

The equivalence between the dual graph picture and the vertex picture is straightforward to show, by considering the dual graphs that are forbidden when applying the conditions of the vertex picture. Condition (1) is violated when an edge's endpoints coincide, or equivalently when multiple vertices of a triangle coincide. The dual graph of such an edge, as well as its general neighborhood, is presented in Fig. 2.2. The hatched area denotes any planar ϕ^3 diagram with one leg, i.e., a planar ϕ^3 *tadpole* diagram of any loop order. The edge e that connects the vertex v to itself is represented in the dual graph as the face v , that meets itself at the edge e . From the illustration, it follows immediately that the existence of such an edge corresponds to the existence of tadpoles in the dual graph. Since condition (1) forbids edges with coinciding endpoints, it follows that it also forbids tadpoles in the dual graph.

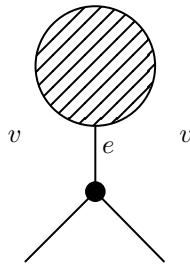


Figure 2.2: The ϕ^3 tadpole diagram in the dual lattice.

For condition (2) a similar argument is made. In general, it is violated when multiple distinct edges share the same pair of vertices as their endpoints, or if two distinct triangles share the same three vertices. The dual of the general case of two edges sharing their endpoints is shown in Fig. 2.3. The dotted area denotes any ϕ^3 diagram with two legs, but excluding the single edge², i.e., a planar ϕ^3 *self-energy* diagram of any loop order. It immediately follows that condition (2) forbids the existence of self-energies in the dual graph.

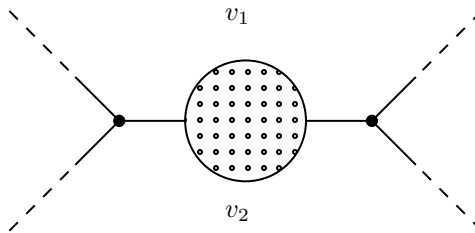


Figure 2.3: The ϕ^3 self energy diagram in the dual lattice.

2.2.2 Applying gravitational action to triangulations

Now that the necessary details of the triangulations have been established, let us consider what it means to calculate the Einstein-Hilbert action on them. Note that the following again only considers combinatorial man without boundary. First, consider the Λ term in the action:

$$S_\Lambda = \frac{1}{2\kappa} \int d^2x \sqrt{g} 2\Lambda. \quad (2.8)$$

The cosmological constant Λ is a constant and can be brought in front of the integral. The remaining integral is the volume integral over the entire manifold. The volume is easily calculated for an equilateral triangulation. Remember that the edge-lengths are set to a , and therefore the volume of each triangle is

²The exclusion of the single edge is to avoid the trivial case where v_1 and v_2 *do* uniquely describe an edge, which is exactly a situation that this illustration is not meant to represent.

set to $\frac{\sqrt{3}}{4}a^2$. The volume of the manifold is then $\frac{\sqrt{3}}{4}a^2N$, where N denotes the number of triangles that make up the manifold.

The curvature term in the action,

$$S_R = -\frac{1}{2\kappa} \int d^2x \sqrt{g} R, \quad (2.9)$$

is less straightforward to apply to triangulations. To make sense of the integral, consider where the Gaussian curvature is located. Since we only consider two-dimensional manifolds, the scalar curvature in the integrand is twice the Gaussian curvature, and it fully captures the curvature of the manifold. The curvature is clearly not located at the interior of the triangles, as they are flat by construction. Furthermore, the curvature is also not located at the edges. To realize this one can employ the fact that bending a surface without stretching leaves the Gaussian curvature unchanged. That leaves the vertices, and the question of what determines the curvature there. A few examples should provide some insight. Consider a vertex, and six triangles meeting at it. Since the triangles are equilateral these together form a hexagon, which is flat. If now less than six triangles meet at a vertex, say four, the resulting shape will be a pyramid with an open base. It is easy to convince oneself that it is impossible to let the pyramid lie in a single plane by only bending along an edge. Consequently, the shape is not flat. A similar argument holds for the case of more than six triangles meeting at a vertex.

The examples above indicate that the curvature, located at the vertices, is related to the degree³ of that vertex. That is indeed the case. A detailed but entry-level exposition of why this is the case can be found in [21], starting at page 62 therein. For completeness, the key points of the argument are reiterated here. Consider a closed curve around a vertex v , enclosing a sufficiently small area dA . Place a vector on the curve, and perform a parallel transportation along the curve. The angle between the parallel transported vector and the original vector is called the deficit angle ϵ . Since all triangles are equilateral, the deficit angle is fully determined by the degree $\deg(v)$ of vertex v :

$$\epsilon_v = 2\pi - \frac{\pi}{3} \deg(v). \quad (2.10)$$

Remember that our goal, S_R , is a surface integral of curvature. Due to the argument before, it is clear that $R = 0$ everywhere apart from the vertices. Thus, to find S_R , one only needs to sum the deficit angle ϵ_v over all vertices in the triangulation T :

$$\int d^2x \sqrt{g} R = \sum_{v \in T} \epsilon_v = \sum_{v \in T} \left(2\pi - \frac{\pi}{3} \deg(v) \right) = 2\pi V - \frac{\pi}{3} \sum_{v \in T} \deg(v), \quad (2.11)$$

where V is a shorthand for $|V(T)|$, the number of vertices in the triangulation. To find the sum of degrees, consider the following argument. Vertex degree is defined as the number of triangle corners meeting in a vertex. Since each triangle has three corners, as its name suggests, each has three "units" of degree to distribute. Consequently, the sum of degrees is equal to three times the number of triangles:

$$\sum_{v \in T} \deg(v) = 3F, \quad (2.12)$$

with F the number of faces (read: triangles) in the triangulation. Finally, it will turn out to be useful to establish a relation between the number of edges E and the number of triangles F . Before gluing, each triangle has three edges. After gluing every edge is associated with exactly one other edge. The result is that after gluing the number of edges is half the number of edges before gluing, providing the following relation:

$$E = \frac{3}{2} F. \quad (2.13)$$

Combining (2.11), (2.12), and (2.13) gives

$$\sum_{v \in T} \epsilon_v = 2\pi \left(V - \frac{\pi}{3} F \right) = 2\pi (V - E + F) = 2\pi \chi, \quad (2.14)$$

³A comment on nomenclature is in order. In graph theory, the *degree* of a vertex denotes the number of vertex neighbors it has. This is closely related to the definition of *degree* used in this work, namely the number of distinct triangles meeting at a vertex. In physics literature, *order* is also a common name for this quantity. However, this clashes with the meaning of *order* in graph theory, denoting the total number of vertices in a graph. Neither is ideal, but *degree* is deemed to be the lesser of the two evils.

where in the last step the formula for the Euler characteristic, $V - E + F = \chi$, was used. This result is not too surprising, since the Gauss-Bonnet theorem states that the l.h.s. of (2.11) should equal $2\pi\chi$. This serves as a check on the arguments presented before.

Combining the simplifications for S_Λ and S_R one finds for the Einstein-Hilbert action applied to a two-dimensional triangulation T :

$$S^{EH}[T] = S_\Lambda[T] + S_R[T] = \frac{1}{2\kappa} \left(2\frac{\sqrt{3}}{4}a^2 N_T \Lambda - 2\pi\chi_T \right) = \lambda N_T - \chi_T/G, \quad (2.15)$$

where in the last step the bare dimensionless cosmological constant λ and gravitational constant G are introduced. The action is fully determined by the triangulation size and its topology, since χ is a topological invariant. The discretized path integral is then

$$Z_a = \sum_{T \in \mathcal{T}} \frac{1}{C_T} e^{-\lambda N_T + \chi_T/G}, \quad (2.16)$$

where C_T denotes the number of elements in the automorphism group of T . Furthermore, \mathcal{T} is the ensemble of triangulations that is considered. Its choice is not unique, and it will be addressed in more detail in 2.3. Recall that the present work only considers triangulations of spherical topology, for which $\chi_T = 2$.

2.2.3 Continuum limit and universality

The continuum limit of (2.16) is obtained by taking the limit of $N_T \rightarrow \infty$, $a \rightarrow 0$, such that the volume $\frac{\sqrt{3}}{4}a^2 N_T$ is conserved. At that point the theory exhibits universality. It is part of a collection of statistical systems characterized by a set of critical exponents. Other theories in the same universality class are the Brownian sphere [22] and Liouville Quantum Gravity [23]. Some notable universal properties are its Hausdorff dimension, $d_H = 4$ [10, 11], and its spectral dimension, $d_s = 2$ [12]. This universality has a practical consequence: any reasonable discretization results in the same continuum limit. The following examples all result in the same continuum limit as the discretization scheme above: quadrangulations, minimal dynamical triangulations [24], and degenerate triangulations [20]. This freedom in discretization does *not* mean that the choice of discretization scheme is irrelevant when it comes to solving the model analytically or numerically. For example, in the case of quadrangulations, there exists a tree-bijection, making them easy to generate [25]. Furthermore, numerical methods do not operate at the continuum limit, and the nature of the discretization choice may influence how numerical results differ from the continuum limit. Different discretization schemes may have varying sensitivity to discretization and finite-size effects [26, 24]. Consequently, comparing numerical results from various approaches can help disentangle properties of the continuum theory from discretization artifacts in numerical results. This property is leveraged in this work, by comparing three triangulation ensembles, each with different local gluing rules. The details of these ensembles are presented in the following section.

2.3 Triangulation Ensembles

The first of the three ensembles that is considered has already been introduced. This ensemble is the combinatorial ensemble \mathcal{T}_C , consisting of the combinatorial triangulations of section 2.2.1. Let us restate its three equivalent definitions, since they serve as a useful contrast to the two other ensembles that will be introduced. For a combinatorial triangulation $T \in \mathcal{T}_C$, it holds that:

1. All edges and vertices of T are *nonsingular*, that is, their *links* are homeomorphic to S^0 and S^1 respectively. This formulation is referred to as the *link picture*.
2. The edges and triangles of T are *uniquely* described by lists of *distinct* vertices. This formulation is referred to as the *vertex picture*.
3. The dual graph of T contains no tadpoles or self-energies. This formulation is referred to as the *dual graph picture*.

The following two sections define two other ensembles, namely the restricted degenerate ensemble \mathcal{T}_{RD} , and the maximally degenerate ensemble \mathcal{T}_{MD} . Both follow the definitions presented in [20].

2.3.1 Restricted degenerate ensemble

The restricted degenerate ensemble \mathcal{T}_{RD} is defined using the vertex picture as follows: edges and triangles are described by lists of distinct vertices, but these lists are no longer necessarily unique. By removing the uniqueness restriction, two distinct edges can share the same pair of endpoints, and two distinct triangles can meet at all three corners. An example of what such a situation might look like is given in Figure 2.4. To illustrate why the aforementioned definition allows this situation, let us go through the vertex lists contained in the edges and triangles, using the (arbitrary) labelling introduced on the right side of Figure 2.4. Both triangles t_1 and t_2 contain the vertices $\{v_1, v_2, v_3\}$. Furthermore, the edges e_1 , e_2 both contain $\{v_2, v_3\}$. Clearly, the vertex lists do not uniquely describe the edges and triangles, but vertices within these lists are distinct.

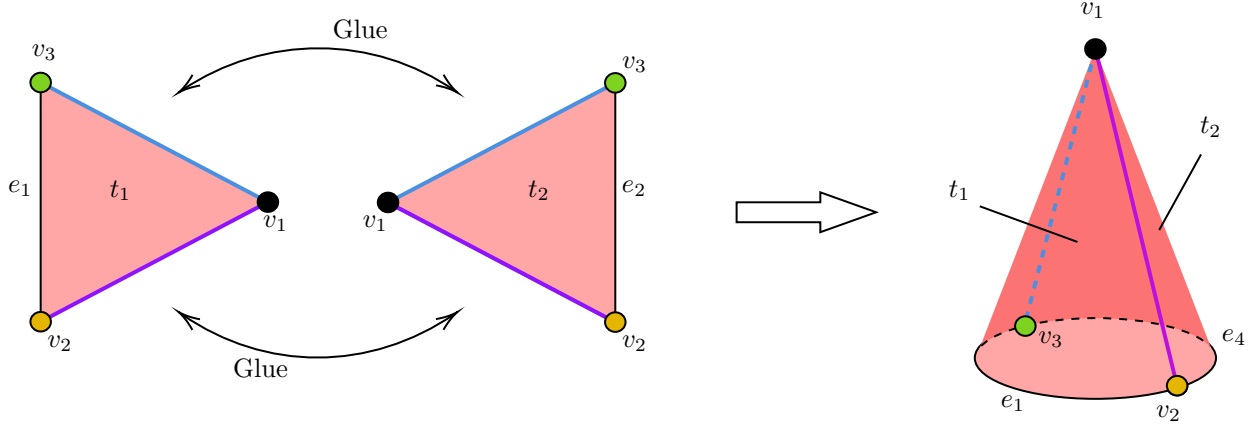


Figure 2.4: An example of a gluing that is possible in \mathcal{T}_{RD} . Coloring is for clarity only.

Consider now what removing the uniqueness restriction means in the link picture. To this end, the example of Figure 2.4 is pictured again in Figure 2.5, now from a top-down view, carrying over the labelling. Additionally, some surrounding triangles are added. Every face is still homeomorphic to the equilateral triangle, even though the edges are bent to make it embeddable in the plane. The link of the cross-marked vertex v_2 , $lk(v_2)$, is depicted in red. It is not homeomorphic to S^1 , due to it including v_1 , and the edge connecting it to v_3 . The cause of this additional edge in the link is the double gluing of triangles t_1 and t_2 . If one were to remove these triangles and glue e_1 to e_2 , the resulting link would be homeomorphic to S^1 . Reversing this argument gives a way to explore what the general link of a vertex in the \mathcal{T}_{RD} ensemble looks like. This exploration is presented in appendix B.

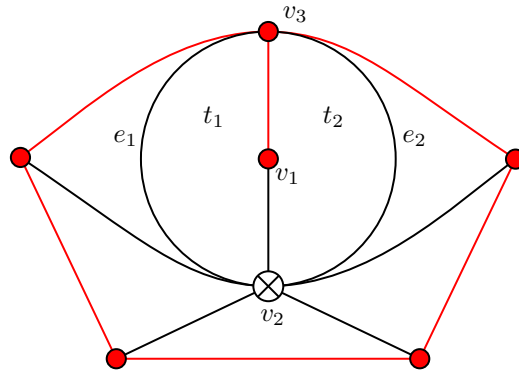


Figure 2.5: Top-down view of the gluing given in Figure 2.4, carrying over its labelling but not its coloring, and with added surrounding triangles. Vertex v_2 is marked with a cross, and its link $lk(v_2)$ is depicted in red.

The degenerate ensemble \mathcal{T}_{RD} is straightforward to formulate in the dual graph picture. Restricted degenerate triangulations are those triangulations whose dual graphs may contain self-energies, but may not contain tadpoles. The equivalence to the vertex picture has been illustrated in section 2.2.1. The distinctness of vertices within the lists ensures the absence of tadpoles. The uniqueness of vertex

lists ensured the absence of self-energies. Consequently, the removal of this restriction allows for the occurrence of self-energies in the dual graph.

2.3.2 Maximally degenerate ensemble

The maximally degenerate ensemble \mathcal{T}_{MD} is characterized in the vertex picture as follows: the lists of vertices describing edges and triangles are not necessarily unique, and the vertices within these lists are not necessarily distinct. Dropping the restriction of distinctness of the vertices allows an edge to have the same vertex on both endpoints. A gluing where such an edge arises is shown in Figure 2.6. Similar to before, an arbitrary labelling is introduced. Using this labelling, let us go through the lists of vertices contained in the edges and triangle of this example. Particularly, notice that edge e_1 contains the vertices $\{v_2, v_2\}$, and the triangle t contains the vertices $\{v_1, v_2, v_2\}$. Evidently, v_2 appears twice in both, so the lists do not contain only distinct vertices.

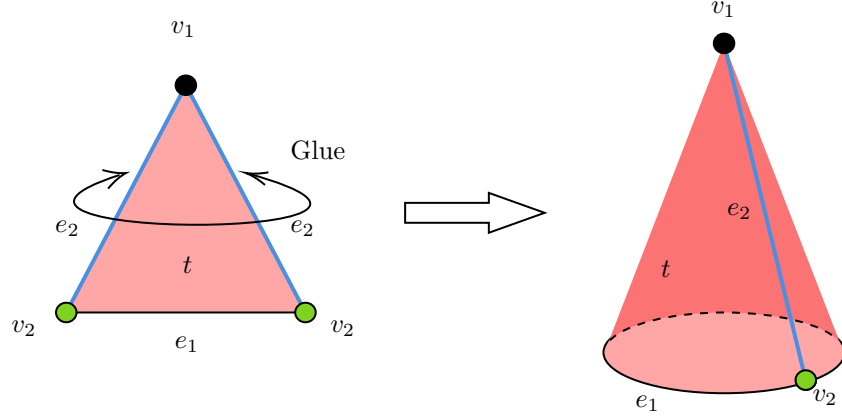


Figure 2.6: An example of a gluing that is possible in \mathcal{T}_{MD} . Coloring is for clarity only.

To see what a situation like this might do to the link, consider again a top-down view. This perspective is shown in Figure 2.7, carrying over the labels of Figure 2.6. Again, the link $lk(v_2)$ is not homeomorphic to S^1 . Furthermore, it is also not connected. Similar to the \mathcal{T}_{RD} case, an exploration of what a general \mathcal{T}_{MD} link looks like is presented in appendix B.

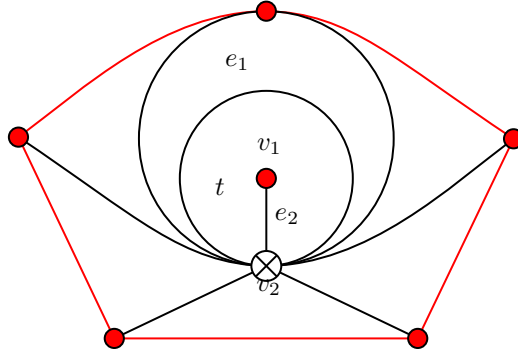


Figure 2.7: Top-down view of the gluing given in Figure 2.6, carrying over its labelling but not its coloring, and with added surrounding triangles. Vertex v_2 is marked with a cross, and its link $lk(v_2)$ is depicted in red.

Again, the \mathcal{T}_{MD} is straightforward to formulate in the dual graph picture. Maximally degenerate triangulations are those triangulations whose dual graphs may contain both self-energies *and* tadpoles. Just like for the restricted degenerate ensemble, the equivalence to the vertex picture has been illustrated in section 2.2.1. The distinctness and uniqueness requirements prevented tadpoles and self-energies respectively. Consequently, removing both restrictions on the vertex lists allows for both tadpoles and self-energies.

2.4 Observables

In section 2.1 it was stated that the path integral is the quantity of interest. More specifically, the aim of this work is to obtain expectation values for observables from the path integral. The expectation value of a quantum observable \mathcal{O} is given by

$$\langle \mathcal{O} \rangle = Z^{-1} \int \mathcal{D}[g_{\mu\nu}^{EU}] \mathcal{O}[g_{\mu\nu}] e^{iS^{EH}[g_{\mu\nu}^{EU}]} . \quad (2.17)$$

Applying all the simplifications for 2D DT presented in section 2.2, and rotating to Euclidean signature, one obtains

$$\langle \mathcal{O} \rangle = Z^{-1} \sum_{T \in \mathcal{T}} \mathcal{O}[T] \frac{1}{C_T} e^{-\lambda N_T} , \quad (2.18)$$

where \mathcal{T} may be any one of the three triangulation ensembles that are given in section 2.3. As mentioned before, the present work only considers triangulations of fixed (spherical) topology, and therefore the χ -term of the action cancels in expectation values, and is not written.

What observable would be of interest? First, let us consider the following requirement, which is already present in the classical theory. Physics must be invariant under diffeomorphisms. In pure gravity, in the absence of physical reference systems, a point in space is not a diffeomorphism-invariant notion, and as such it follows that a field evaluated at a point is not a diffeomorphism-invariant observable. This problem can be addressed by not looking at a single point, but instead considering integrals over the whole manifold. Additionally, the piecewise linear manifolds considered present more hurdles to overcome. Say, one is interested in curvature. One may be tempted to turn to the classical approach of constructing the Riemann tensor and contractions using the metric and its derivatives. However, this approach breaks down when applied to piecewise linear manifolds. They are not differentiable, so there is no access to the usual tensor calculus tools. This motivated the approach to curvature in section 2.2. Does this mean that the question of defining curvature on piecewise linear manifold is solved? The answer is no. One must be careful when trying to apply the deficit angle prescription to piecewise linear manifolds of higher dimensions. While that case is not directly considered in this work, it is part of the bigger picture, namely working with the full 4D theory. In 2D, equation (2.14) evaluates to a constant. However, in dimensions higher than 2 the integrated scalar curvature does not, and it diverges in the continuum limit, with no obvious renormalization prescription [6].

Despite the aforementioned challenges, there is still a multitude of interesting observables to study. To name some examples, measuring return probabilities in diffusion processes provides an estimate for the spectral dimension, and likewise ball volume measurements provide an estimate for the Hausdorff dimension [27]. When it comes to curvature, one could turn to the recently introduced Quantum Ricci Curvature (QRC) [5]. Since measurements of this quantity are central to this work, its details are presented in the following section.

2.4.1 Quantum Ricci Curvature

The quantum Ricci curvature is based on a comparison of the distance between spheres to the distance between their centers. This ratio captures curvature quasi-locally⁴. This quantity is first introduced in the setting of smooth Riemannian manifolds, but one should keep the eventual application to piecewise flat manifolds in mind. The construction, presented in Figure 2.8, is as follows. Consider a Riemannian manifold (M, g) of dimension D , and two nearby points p, p' on it, separated by a geodesic distance δ . These points serve as the centers of two geodesic spheres of radius ϵ , S_p^ϵ , and $S_{p'}^\epsilon$. Let q denote a point on S_p^ϵ , and likewise q' on $S_{p'}^\epsilon$. A notion of distance between the spheres is needed. One could make use of parallel transport to uniquely associate a point q' to each q in the following way: consider the initial vector of the unique geodesic from p to q . Parallel transport it to p' , and let q' be the point that lies a distance ϵ along the unique geodesic with the parallel transported vector as initial vector. The sphere distance is then the average distance between such point pairs. This prescription is well-suited to smooth applications with sufficiently small ϵ and δ , where the explicit computation of geodesics and parallel transport is feasible. However, this parallel transport prescription is not suited for piecewise flat manifolds. The natural choice here is to only consider distances between vertices on the spheres. Generally, one cannot make a one-to-one pairwise association between the vertices on the sphere, as the

⁴Quasi-local in the sense that the QRC is sensitive to the curvature in the neighborhood involved in the construction. In a typical application this area is not a single point.

number of vertices in the spheres is not necessarily equal. This problem can be circumvented by using a slightly different prescription. Instead of incorporating the distance to one unique q' for each q in the average, the distance between each q and *every* point on $S_{p'}^\epsilon$ is considered in the average. This *average sphere distance* between a pair of spheres is then defined as

$$\bar{d}(S_p^\epsilon, S_{p'}^\epsilon) = \frac{1}{\text{vol}(S_p^\epsilon)} \frac{1}{\text{vol}(S_{p'}^\epsilon)} \int_{S_p^\epsilon} d^{D-1}q \sqrt{h} \int_{S_{p'}^\epsilon} d^{D-1}q' \sqrt{h'} d(q, q'), \quad (2.19)$$

where h, h' denote the determinants of the induced metrics on the spheres, and $d(q, q')$ the geodesic distance between points q and q' . Using this prescription, the quantum Ricci curvature $K_q(p, p')$ is defined by

$$\frac{\bar{d}(S_p^\epsilon, S_{p'}^\epsilon)}{\delta} = c_q(1 - K_q(p, p')), \quad (2.20)$$

where c_q is a non-universal constant. For simplicity, ϵ is hereafter set equal to δ . Consequently, K_q now captures the curvature at a certain coarse-graining scale δ . The left-hand side of (2.19), or $K_q(p, p')$, does not fit the criteria for a diffeomorphism-invariant observable, which were laid out in the previous section. It is evaluated at a given pair of points, which is not a diffeomorphism-invariant notion. To make a diffeomorphism-invariant observable, $\bar{d}(S_p^\delta, S_{p'}^\delta)$ is averaged over all point pairs p, p' on the manifold, subject to the constraint $d(p, p') = \delta$. The resulting quantity

$$\frac{\bar{d}_{av}(\delta)}{\delta} = c_{av}(1 - K_{av}(\delta)), \quad (2.21)$$

as a function of δ , is called the curvature profile [28]. The constant c_{av} is given by $\lim_{\delta \rightarrow 0} \bar{d}_{av}(\delta)/\delta$. In [5], the curvature profile is determined for, among others, smooth constantly curved 2D manifolds⁵. Here, K_{av} showed the qualitative behavior expected for scalar curvature. Namely, $K_{av} > 0$ (< 0) for positively (negatively) curved spaces, and $K_{av} = 0$ in flat space.

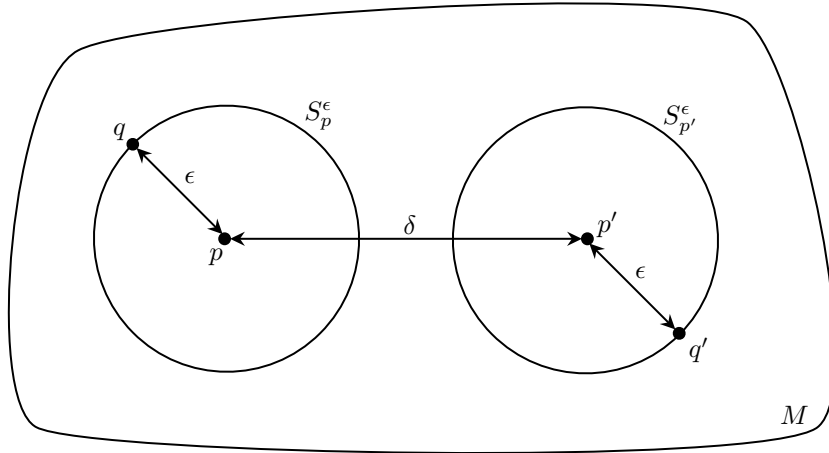


Figure 2.8: The construction needed to determine quantum Ricci curvature. This is obtained by comparing the distance between the ϵ -spheres $S_p^\epsilon, S_{p'}^\epsilon$ to the distance δ between their centers p, p' .

Application to smooth spheres

An expression for the curvature profile for a smooth constantly curved space of any dimension D can be given in terms of an exact integral. These curves form a useful benchmark for curvature profiles of non-smooth settings, such as the dynamical triangulations that are the subject of the present work. Of particular interest to us are the curvature profiles of D -spheres with radius ρ . Motivated by the anomalous fractal dimension of 2D EDT, curvature profiles of D -spheres with $D \geq 2$ are considered. Specifically, the curvature profiles of D -spheres of dimensions $D = 2, 3, 4, 5$ have been determined in [7]. No closed form for these curves was found, and additionally the exact integral expressions were not given

⁵On smooth constantly curved spaces no manifold averaging is needed. The curvature profile is equal to the normalized average sphere distance $\bar{d}(S_p^\delta, S_{p'}^\delta)/\delta$ between any δ -separated point pair p, p' .

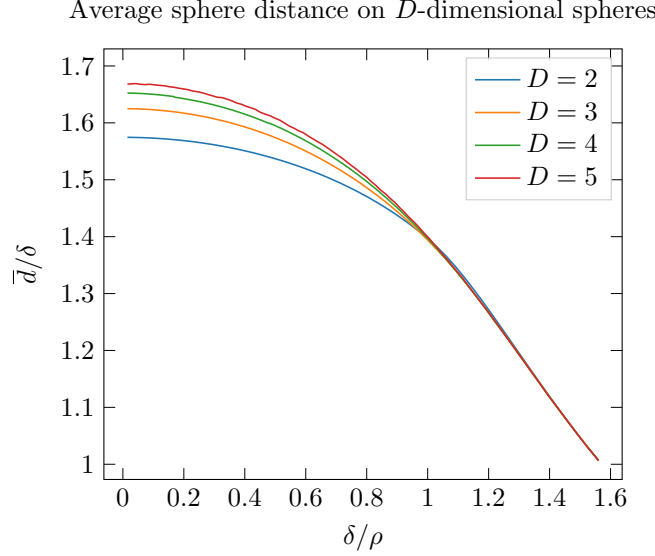


Figure 2.9: Curvature profiles for D -spheres as a function of δ rescaled by the curvature radius ρ , with $D = 2, 3, 4, 5$. Results are numerical estimates of the exact integral expressions found in appendix C.

in [7] for $D \geq 3$. Therefore, the derivation of the exact integral expressions for these curves is repeated. Details of this derivation are presented in appendix C. The numerical estimates for these curves are presented in Figure 2.9. These curves are shown as a function of δ/ρ , since the curvature profile for a sphere of any radius ρ can be obtained from the curvature profile of the unit sphere by a rescaling $\delta \rightarrow \delta/\rho$.

Application to triangulations

Up to this point, the quantum Ricci curvature has been introduced and applied only on smooth manifolds. Let us now consider the piecewise flat implementation. Note that the construction of the average sphere distance in equation (2.19) is purely geometric. This property makes it relatively straightforward to implement in a piecewise flat setting. To make this adaptation the following identifications are made:

- Points p, p', q, q' are vertices of the triangulation,
- $d(p, p')$ is the *link distance*⁶, the shortest distance along edges from p to p' ,
- S_p^δ is the collection of vertices at link distance δ from p ,
- $\text{vol}(S_p^\delta)$ is the number of vertices in S_p^δ ,
- and integrals over the spheres $\int_{S_p^\delta} d^{D-1}q \sqrt{h}$ become sums over the sphere's vertices $\sum_{v \in S_p^\delta}$.

Similar to the smooth prescription, the curvature profile of a triangulation T is defined by a manifold average:

$$\frac{\bar{d}_T(\delta)}{\delta} = \frac{1}{\delta} \frac{1}{n_T(\delta)} \sum_{p \in T} \sum_{p' \in T} \bar{d}(S_p^\delta, S_{p'}^\delta) \delta_{d(p, p'), \delta}, \quad (2.22)$$

where $\delta_{a,b}$ is the Kronecker delta, and $n_T(\delta) = \sum_{p \in T} \sum_{p' \in T} \delta_{d(p, p'), \delta}$ a normalization factor equal to the number of point pairs separated by link distance δ in the triangulation T . It should be noted that extracting $K_{av}(\delta)$, similar to (2.21), is not completely straightforward. The limit $\delta \rightarrow 0$ is not meaningful in this discrete piecewise flat implementation, and as a consequence it is not immediately clear how one should define c_{av} . Details on how to address this issue are presented in chapter 5. An application of curvature profiles on regular lattices, and triangulations that do not deviate too much from smooth spaces can be found in [5]. Application to 2D Causal Dynamical Triangulations (CDT) can be found in [8]. The

⁶This usage of the word *link* clashes with the definition of *link* given in section 2.2.1. However, in physics literature, the definition of distance as the length of the shortest path between vertices along edges is commonly referred to as *link distance*. Where context does not suffice, any ambiguity will be clarified.

original application to 2D EDT [7] is of particular interest for the present work. These measurements are replicated in the present work, their details are reiterated in chapter 5. Briefly summarizing the content of [7]: a comparison of curvature profiles of 2D EDT to the profiles of smooth D-spheres of Figure 2.9, resulted in the conclusion that the 2D EDT curvature profile has the closest resemblance to the curvature profile of a 5-sphere. This result was not necessarily conclusive, due to the qualitative similarities of the aforementioned D-sphere curves. Furthermore, while there is not an a priori expectation of what the best fit D should be, 5 is not in line with either the topological, Hausdorff, or spectral dimension, thus warranting the deeper investigation in the present work.

2.5 Sampling triangulations

This section will explain how one goes about evaluating an expression like (2.18) in practice. The expectation value $\langle \mathcal{O} \rangle$ of some observable \mathcal{O} is approximated by sampling the ensemble \mathcal{T} at hand n times at random, with repetition. These sample triangulations are labelled T_1, \dots, T_n ⁷. The average of the observable \mathcal{O} evaluated on these samples,

$$\bar{\mathcal{O}}_n = \frac{1}{n} \sum_{i=1}^n \mathcal{O}[T_i], \quad (2.23)$$

approximates the expectation value $\langle \mathcal{O} \rangle$, such that

$$\lim_{n \rightarrow \infty} \bar{\mathcal{O}}_n = \langle \mathcal{O} \rangle. \quad (2.24)$$

This equality only holds if the triangulations are sampled with the correct distribution.

The triangulations are difficult to sample directly, that is, by generating them individually from a set of random numbers. A more efficient way of sampling triangulations is by using a Markov chain Monte Carlo (MCMC) algorithm. The general idea here is to generate each new sample from the last sample, by applying random updates to it. A clear introduction to MCMC is found in [29], an extensive overview of applications of Monte Carlo techniques in physics can be found in [30].

First, the updates that are applied to the triangulations are presented. Subsequently, the method for ensuring the correct distribution of the samples is given. The triangulations are updated by performing an edge flip. How this update acts locally on a triangulation is shown in Fig. 2.10. It has been shown that the edge flip is ergodic when applied to combinatorial triangulations. In other words, any triangulation T_a in the combinatorial ensemble can be obtained from any T_b in the combinatorial ensemble by applying a finite number of edge flips, where all triangulations that are obtained during this process are also in \mathcal{T}_C . The chosen update being able to fully explore the space of states is a requirement for obtaining the correct distribution. Thus, to be able to use the edge flip to sample the degenerate ensembles, it needs to be ergodic in these ensembles as well. In appendix D it is shown that the edge flip is indeed ergodic in the degenerate ensembles.

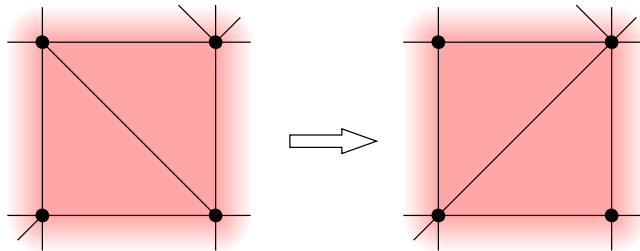


Figure 2.10: The edge flip update.

Next, let us turn to the matter of ensuring the samples are correctly distributed. To this end, the Metropolis-Hastings algorithm is used [31, 32]. An update is proposed at random, and accepted or rejected with a certain acceptance probability. This acceptance probability depends on the desired probability distribution of the samples and the probability of proposing the update. If the edge that is to

⁷The subscript here identifies the sample, but does not refer to a specific triangulation. As such, it is perfectly fine for the number of samples n to exceed the number of triangulations in the ensemble. This is relevant when triangulation size N is fixed, in which case the ensemble is finite.

be flipped is chosen uniformly at random from the edges of the triangulation, the acceptance probability that gives the desired distribution of the samples is remarkably simple for all three ensembles. If \mathcal{T} is one of the three ensembles considered in the present work, an edge flip is accepted if the resulting triangulation is in \mathcal{T} , and rejected otherwise.

At this point, the method for how to obtain a new triangulation sample from an existing one has been established. However, there are still practical matters that need to be addressed. First, the process of creating a new sample from an old one needs to start somewhere. A method for constructing an initial triangulation is needed. Second, this initial triangulation may be atypical, that is, observables measured on it may be far away from their expectation value. If one starts sampling the chain of triangulations here, a bias could be present in the averages of observables. Therefore, a number of edge flips is performed before samples are taken from the chain. This number of edge flips is referred to as the *equilibration time*. Lastly, two triangulations related by a single edge flip are highly correlated. To avoid this, a fixed number of edge flips are performed between every triangulation sample. This number of edge flips is referred to as the *autocorrelation time*. The methods used to address these issues are presented in chapter 3.

Chapter 3

Monte Carlo practicalities

In section 2.5, the use of Markov chain Monte Carlo methods to sample triangulations was presented. At the end of this section, three practical considerations were noted:

1. *Initialization:* The chain of triangulations has to start somewhere. One must choose a method of constructing an initial triangulation.
2. *Equilibration:* The initial triangulation may be atypical. To avoid bias from sampling these atypical triangulations, a number of updates must be performed before sampling triangulations from the chain.
3. *Autocorrelation:* Subsequent triangulations, that is, those related by a single edge flip, are almost identical. As a consequence, there likely are large correlations between measurements on subsequent triangulations.

This chapter addresses these three matters.

3.1 Initialization

As mentioned before, the chain of triangulations has to start somewhere. The present section provides a method to create an initial state.

Any combinatorial triangulation of the correct size will be a valid initialization in all three ensembles. This conclusion follows from the ergodicity of the edge flip in the three ensembles, and the fact that \mathcal{T}_C is a subset of both \mathcal{T}_{RD} and \mathcal{T}_{MD} .

The following procedure for constructing initial triangulations is chosen for its ease of implementation. Start with four triangles, glued together such that they form the surface of a tetrahedron.

If the current triangle number is lower than the desired triangle number, pick a triangle randomly, and perform the (1,3)-move as presented in Fig. 3.1. This move inserts three triangles in the place of the selected triangle. As a consequence of this move, the triangle number is increased by two. The random insertions are repeated until the triangulation is of the correct triangle number.

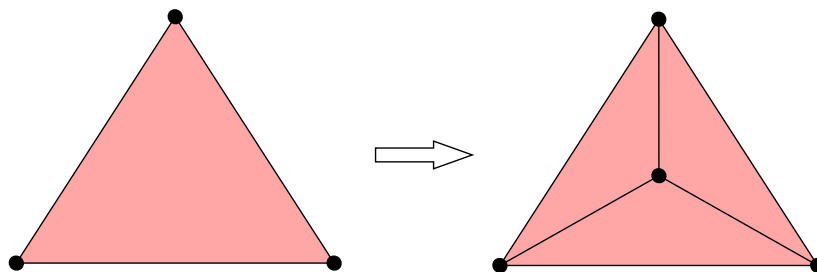


Figure 3.1: The (1,3)-move in two dimensions.

Using this procedure, only triangulations of even triangle number can be created. However, this limitation is not problematic. It follows from the formula for the Euler characteristic that any triangulation in the ensembles that are considered must have an even number of triangles. Therefore, only being able to initialize a triangulation of even triangle number is sufficient.

3.2 Equilibration

The initial triangulations described in the previous section may be atypical. That is, observables measured on these triangulations may be far from their ensemble expectation value. In that case, if one were to start sampling triangulations directly after initialization, a large bias may be imparted on the average of observables measured on these sample triangulations. This bias is avoided by simply waiting with sampling triangulations until a certain number of updates has been performed. The number of updates is called the equilibration time τ_e . The equilibration time is not universal, and may depend on triangulation size and ensemble. The present section aims to estimate sufficient equilibration times for the various ensembles and triangulation sizes that are considered in the present work.

To this end, triangulations are sampled from triangulation Markov chains at regular intervals, starting at the initial triangulation. More precisely, triangulations are sampled for all three ensembles and sizes $N = 10k, 100k, 500k$, and $1000k$. Starting with the initial triangulation, 200 samples are taken from each chain, where a sweep of updates is performed between each sample. One sweep corresponds to a number of edge flips equal to the number of triangles in the triangulation at hand. The histogram of vertex degrees of each sample triangulation is measured, and normalized to obtain the vertex degree distribution.

The results for triangulations with $N = 500k$ triangles are presented in Fig. 3.2 as follows. The initial vertex degree distribution of the initial triangulation is shown in blue. Additionally, the average of the vertex degree distributions of the last 150 samples is shown in orange. Finally, the vertex degree distribution is known analytically in the limit of the triangle number $N \rightarrow \infty$ for the combinatorial ensemble:

$$P(q) = 16 \left(\frac{3}{16} \right)^q \frac{(q-2)(2q-2)!}{q!(q-1)!}, \quad (3.1)$$

where q denotes the vertex degree [33]. This distribution is shown in Fig. 3.2a. For all three ensembles, the initial distribution is markedly different from the average distribution taken from the later triangulation samples. Furthermore, for the combinatorial ensemble, the average vertex distribution of the later triangulation samples matches the theoretical large triangulation distribution of equation (3.1).

Next, the evolution of the vertex degree distribution with simulation time is studied in more detail. It is useful to capture the similarity of two distributions in a single number. The Wasserstein 1-distance W_1 , also known as the earth mover's distance, is used for this purpose. In general, the Wasserstein p -distance is a metric if $p \geq 1$ [34]. In the case of 1-dimensional distributions, which is the case at hand, the Wasserstein 1-distance has a simple formula: given distributions μ_1 and μ_2 , and their respective cumulative distribution functions $C_1 = \int_{-\infty}^x \mu_1(x') dx'$ and C_2 likewise, the Wasserstein 1-distance between these distributions is

$$W_1(\mu_1, \mu_2) = \int_{\mathbb{R}} |C_1(x) - C_2(x)| dx. \quad (3.2)$$

Let P_1, P_2, \dots, P_{200} denote the vertex degree distributions of the 200 sample triangulations from a single Markov chain. For each of the aforementioned sizes and ensembles, the distance $W_1(P_i, P_{200})$ is determined for $i = 1, 2, \dots, 200$. In other words, each distribution is compared to the final distribution that is measured. These distances are shown in Fig. 3.3. Two observations are made:

1. The shape of the curves shows that for all sizes and ensembles considered, the initial triangulation is indeed atypical. The distance to the last vertex degree distribution P_{200} is initially large. However, performing edge flips eventually provides triangulations whose vertex degree distributions are close to P_{200} .
2. The curves for different sizes overlap in their initial decline. It follows that the number of updates needed to move away from the atypical initial triangulation, measured in sweeps, does not depend on triangle number. In other words, the number of edge flips needed for equilibration is proportional to the triangulation size.

It should also be reiterated that the curves in Fig. 3.3 are each based on a single Markov chain. To obtain a reliable estimate for the equilibration time, measurements from 20 Markov chains at $500k$ are combined, for all three ensembles. From each chain, 100 triangulations are sampled. Between each sample one sweep of edge updates is performed, and the first sample is the initial triangulation of the chain. The histogram of vertex degrees is determined for all triangulation samples. As a result, 20 vertex degree histograms are obtained at each sweep number. These 20 histograms are added and normalized, giving an average vertex degree distribution at each sweep number ranging from 0 to 100. Again, the

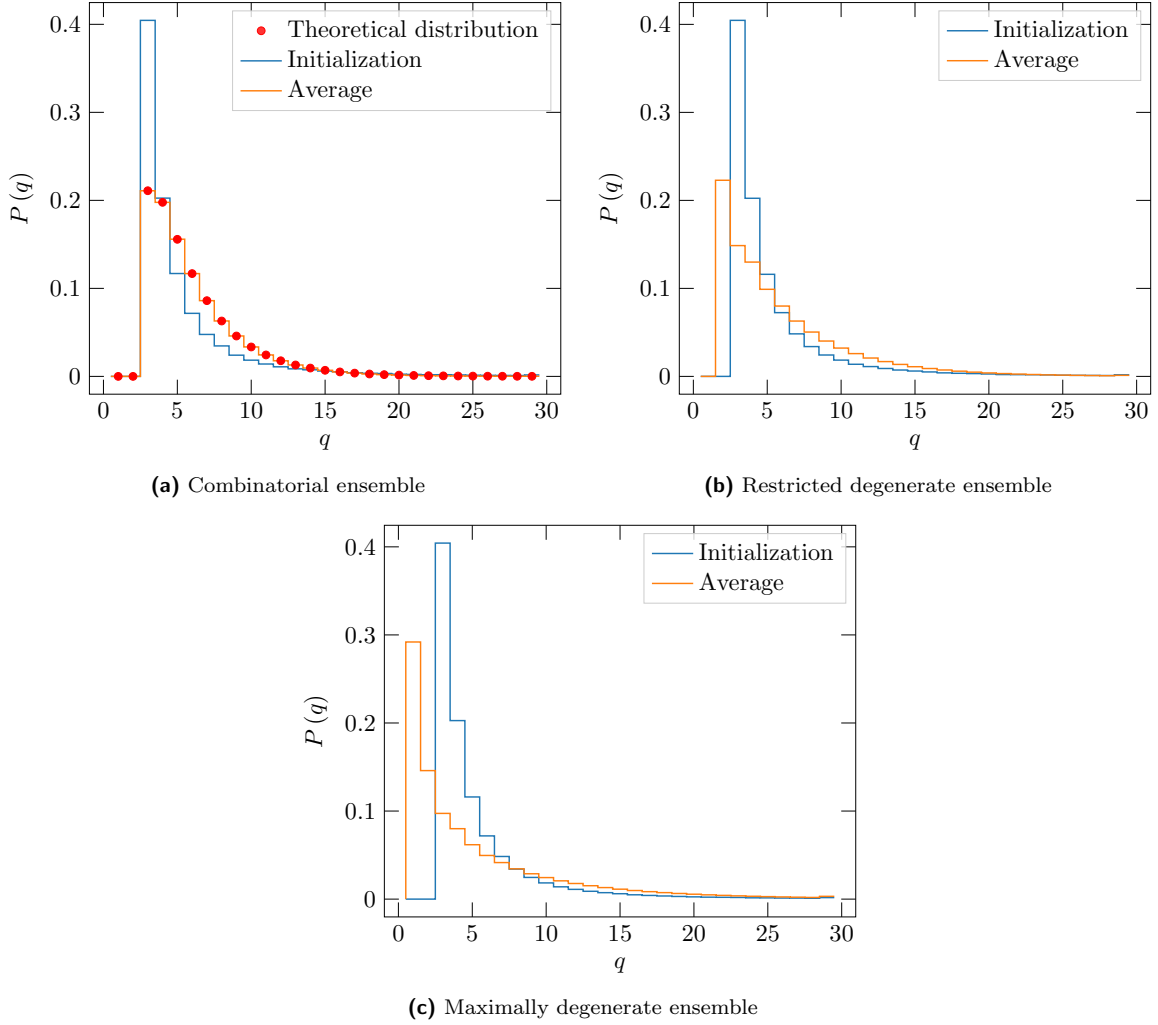


Figure 3.2: Vertex degree distributions $P(q)$ for the three ensembles, for triangulations of size $N = 500k$. The distribution of the initial triangulation is shown in blue, the average distribution of the last 150 samples is shown in orange. Additionally, in (a), the known vertex distribution for combinatorial triangulations in the limit $N \rightarrow \infty$, given in equation (3.1), is shown in red.

distance to the final distribution is determined at each sweep number. These distances are shown in Fig. 3.4, for the three ensembles. All three curves reach a plateau near 0 well before 100 sweeps have passed since initialization. An equilibration time of 100 sweeps is considered sufficient for all sizes and ensembles that are considered in the present work. Although this is a high estimate, equilibration is only performed once per Markov chain. Consequently, the penalty in computation time that is caused by a high estimate for the equilibration time is negligible. Note that despite this choice of 100 sweeps for the three ensembles, the actual equilibration times observed for the three ensembles are shortest for the combinatorial ensembles, and longer for the more degenerate ensembles.

3.3 Autocorrelation

A single edge flip leaves a triangulation nearly unchanged. Measurements on triangulations that are related by a single edge flip are therefore highly correlated. It is not necessarily incorrect to sample after each edge flip, since the resulting correlations can be addressed properly in error estimation. However, the approach of sampling after every edge flip is not suitable to the simulations performed in the present work. The average sphere distance introduced in section 2.4.1 is computationally expensive when compared to the edge flip. Therefore, thinning is used: sample triangulations are sampled from the Markov chain at regular, longer intervals, such that each sample can be considered uncorrelated to the other samples. To determine a suitable interval between samples, the autocorrelation time is studied.

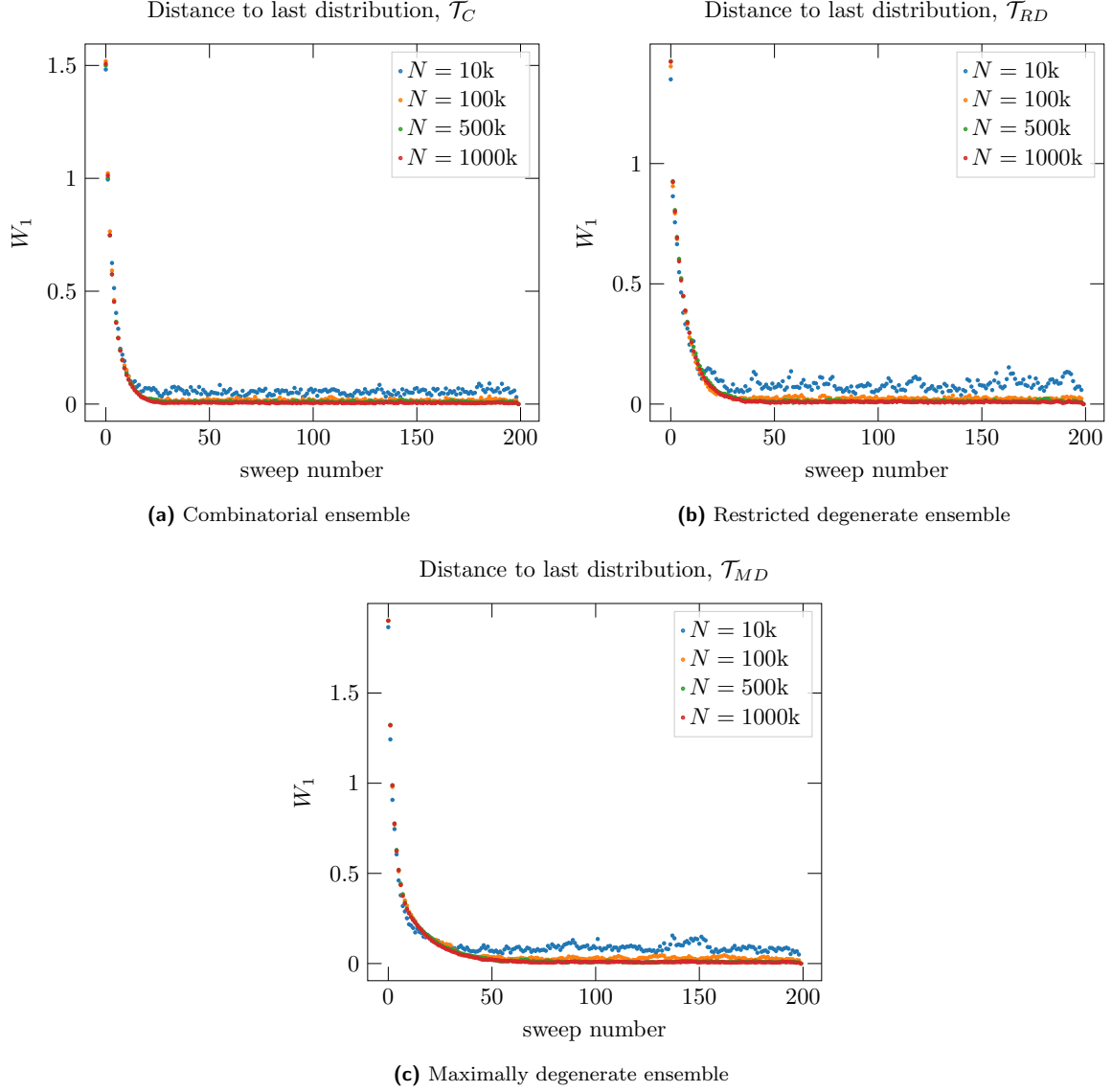


Figure 3.3: The Wasserstein 1-distance W_1 of vertex degree distributions P_i to the vertex degree distribution P_{200} measured at 200 sweeps after initialization, for all three ensembles and sizes $N = 10k, 100k, 500k, 1000k$.

To this end, an observable \mathcal{O} , to be specified later in this section, is measured on a series of n triangulation samples T_i , taken from a single Markov chain. Let \mathcal{O}_i denote the observable \mathcal{O} , evaluated on T_i . The sample autocovariance $\bar{\gamma}(t)$ is given by

$$\bar{\gamma}(t) = \frac{1}{n} \sum_{i=1}^{n-t} (\mathcal{O}_i - \bar{\mathcal{O}}) (\mathcal{O}_{i+t} - \bar{\mathcal{O}}), \quad (3.3)$$

where $\bar{\mathcal{O}}$ denotes the average of \mathcal{O}_i . In principle, t can range from 0 to $n - 1$. However, $\bar{\gamma}(t)$ is calculated using $n - t$ samples for a given t , in practice t should not be too close to n . In the present work, $t < 0.8 * n$ is deemed to be sufficient. The sample autocorrelation $\bar{\rho}$ is given by [29]

$$\bar{\rho}(t) = \frac{\bar{\gamma}(t)}{\bar{\gamma}(0)}. \quad (3.4)$$

The autocorrelation time τ_a is found by assuming $\bar{\rho}(t)$ decays exponentially, with τ_a as its time constant.

In the present work, the vertex degree distribution is used to determine the sample autocorrelation. However, it is not possible to substitute the vertex degree distribution directly for \mathcal{O} in equation (3.3), since it is not a number. Let $P_i(q)$ denote the vertex degree distribution of the triangulation sample T_i , where q denotes the vertex degree. Furthermore, let $P_f(q)$ be the last measured vertex degree

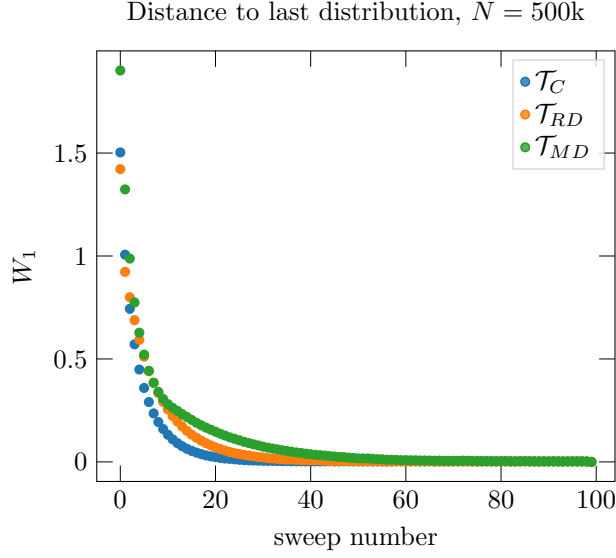


Figure 3.4: The Wasserstein 1-distance W_1 of average vertex degree distributions to the average vertex degree distribution measured at 200 sweeps after initialization, at triangulation size $N = 500k$, and for all three ensembles.

distribution. For each triangulation sample T_i , the distance Δ_i of its vertex degree distribution to the average,

$$\Delta_i = W_1(P_i, P_f), \quad (3.5)$$

is determined. This distance Δ is substituted for \mathcal{O} in equation (3.3). This way, a sample autocorrelation is found based on the vertex degree distribution.

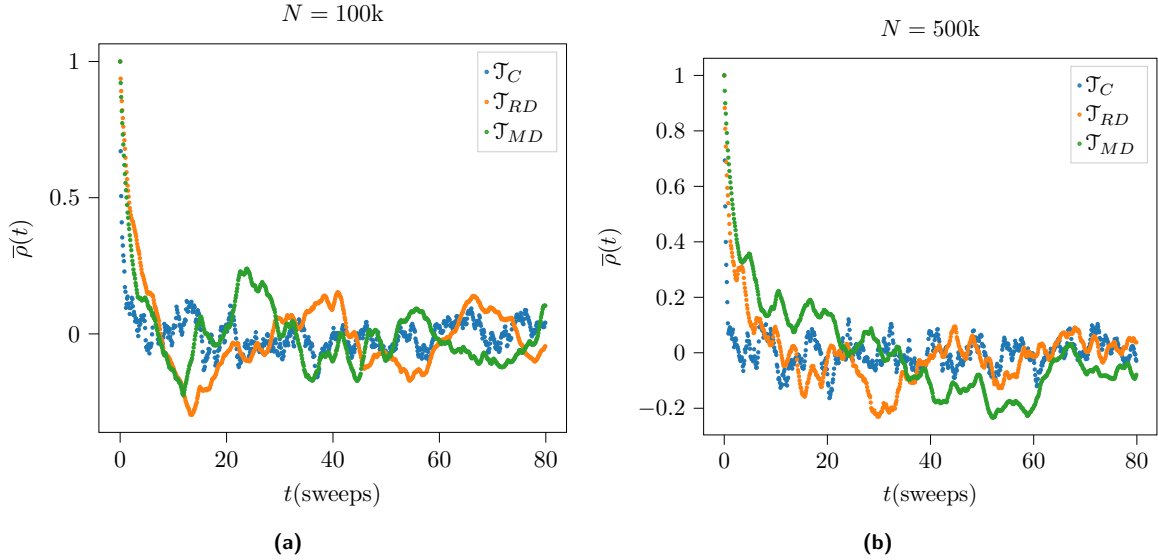


Figure 3.5: Sample autocorrelation $\bar{\rho}(t)$ based on the vertex degree distribution, as a function of simulation time t in sweeps, for sizes $N = 100k, 500k$, and the three ensembles.

Triangulation Markov chains are sampled for sizes $100k$ and $500k$, and for all three ensembles. Each chain is equilibrated first, with the equilibration time found in section 3.2. Afterwards, 1000 sample triangulations are taken with $1/10$ sweep intervals. The sample autocorrelation $\bar{\rho}$ based on the vertex degree distribution of these triangulation samples is determined, following the aforementioned prescrip-

tion. This sample autocorrelation is presented in Fig. 3.5, for the sizes and ensembles considered.¹ In all cases of size and ensemble, $\bar{\rho}$ shows a sharp initial drop, followed by a noisy plateau around $\bar{\rho} = 0$.

Considering the relative computational inexpensiveness of the edge flips compared to measuring average sphere distance, one can increase the thinning without a significant increase in computation time. In other words, the autocorrelation time can safely be overestimated. For the sizes and ensembles considered in the present work, an interval of 50 sweeps between samples is deemed to be sufficient for the samples to be considered uncorrelated.

¹Even though the simulation time during which samples have been taken covers 100 sweeps, only 80 sweeps are shown in Fig. 3.5. Due to the nature of eq. (3.3), the value of $\bar{\gamma}(t)$ is based on $n - t$ measurements. Therefore, the data points for later values of t are less reliable. Placing the cut-off for the range of t at $t = 80$ sweeps is deemed sufficient to remove these points.

Chapter 4

Hausdorff Dimension

As mentioned before in section 2.2.3, the Hausdorff dimension of 2D EDT is known, and backed up with a wealth of evidence from numerical experiments. The methods in this section are not new, they follow [11] closely. Nevertheless, measurements of the global Hausdorff dimension in 2D EDT are presented here, since they provide helpful insights. First, they give another validation for the implementation of the algorithm for sampling the triangulations. Additionally, they provide a direct comparison of sphere growth-based measurements in the three ensembles. This may give insight into the sensitivity to discretization effects and finite-size effects, which may not be the same for different ensembles.

4.1 Methods

Recall that the Hausdorff dimension d_H describes how the volume $|B_r|$ of a ball scales with its radius r :

$$|B_r| \propto r^{d_H}, \quad (4.1)$$

to leading order in r . Here, a ball of radius r is defined as the set of all points at a distance that is at most r to the ball's center. The relation of equation (4.1) holds for 2D EDT with $d_H = 4$ in the limit $r \rightarrow 0$. Contrary to flat 2-dimensional space, the boundary of a ball in 2D EDT is not necessarily one single connected component. Furthermore, for finite-sized triangulations the scaling of equation (4.1) is only obtained in the limit $N \rightarrow \infty$, where N denotes the number of triangles in the triangulation. For obvious reasons, this limit cannot be reached by our simulations. Therefore, the finite-size scaling approach outlined in [11] is used. This approach is briefly presented here.

Let $\rho_N^{\mathcal{T}}(r)$ denote the probability that two randomly chosen vertices are a distance r apart, on a triangulation of size N and in the ensemble \mathcal{T} . Define the renormalized distance $x = N^{-1/d_H}r$. Now, assume that the following limit holds:

$$\lim_{N \rightarrow \infty} N^{1/d_H} \rho_N^{\mathcal{T}}(N^{1/d_H}x) = \rho^{\mathcal{T}}(x). \quad (4.2)$$

Then, the rescaling necessary to let the curves $\rho_N^{\mathcal{T}}(r)$ fall on top of each other should approach that of eq. (4.2) for large triangle number N . Instead of the entire curve, one could also consider the peak height or location of $\rho_N^{\mathcal{T}}(r)$, which should follow a similar rescaling. These alternative approaches are discussed in more detail in section 4.3.

Measuring $\rho_N^{\mathcal{T}}(r)$ is straightforward. It is closely related to the expectation value $\langle |\partial B_r| \rangle$ of the boundary length of a ball of radius r , centered on a randomly chosen vertex on a triangulation of size N and ensemble \mathcal{T} :

$$\rho_N^{\mathcal{T}}(r) = \frac{\langle |\partial B_r| \rangle_{N,\mathcal{T}}}{N}, \quad (4.3)$$

where N is a natural normalization, since $\int_0^\infty dr |\partial B_r| = N$. To estimate this expectation value, ball boundary lengths are measured on triangulations of sizes $N = 20k, 40k, 60k, 80k, 100k, 120k, 160k, 250k, 500k$, and $1000k$. A total of 10^4 sample triangulations are used for each size and ensemble. On each triangulation a vertex is chosen uniformly, and centered at this vertex a ball is grown layer by layer. Its boundary length is measured every time a new layer is added. This is continued until the volume of the ball is equal to the triangulation volume. The ball boundary length expectation value as function of r is then approximated by averaging the measurements for each size N and ensemble \mathcal{T} .

4.2 Results

The resulting approximations of the ball boundary length expectation value $\langle |\partial B_r| \rangle_{N,\mathcal{T}}$ are presented in Fig. 4.1. Results are shown for all sizes considered, and for all three ensembles. Comparing to existing measurement (for example [35]), the curves are of the expected shape: slightly skewed to the right. Note also that the curves for the restricted degenerate ensemble are peaked slightly sharper than the curves for the combinatorial ensemble, and likewise the curves for the maximally degenerate ensemble are peaked slightly sharper than those for the restricted degenerate ensemble.

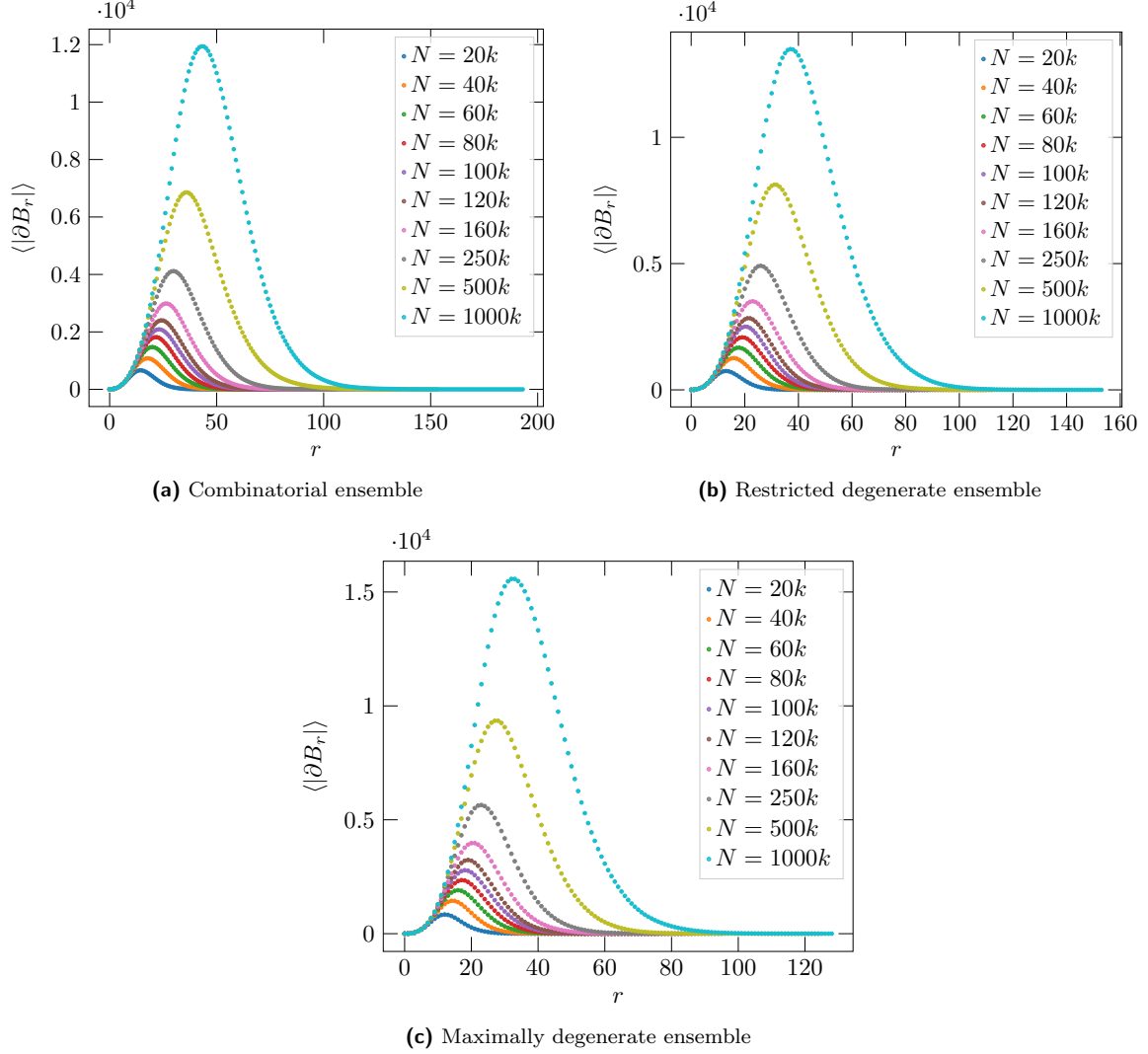


Figure 4.1: Ball boundary length expectation value $\langle |B_r| \rangle$ as a function of radius r . Measurements are presented for various different triangulation sizes N , and for all three ensembles.

Following [11], the resulting distributions are “collapsed” to a reference distribution. This reference distribution is chosen to be the distribution $\rho_{N_0}^{\mathcal{T}}(r)$ measured for the largest triangulation size $N_0 = 10^6$. Then, $k_N^{-1} \rho_N^{\mathcal{T}}(k_N^{-1}x)$ can be fitted to $k_{N_0}^{-1} \rho_{N_0}^{\mathcal{T}}(k_{N_0}^{-1}x)$, with $k_{N_0} = 1$. Note that, following [11], data points where $\rho_N^{\mathcal{T}}(r)$ lies below one fifth of its maximum are excluded from this fit, as well as any following curve collapse fits.

To improve the collapse, a fixed shift s in r is introduced: $r \mapsto r - s$. This shift is determined by first collapsing $k_N^{-1} \rho_N^{\mathcal{T}}(k_N^{-1}(x + s_N) - s_N)$ to $\rho_{N_0}^{\mathcal{T}}(x)$. For each ensemble, the constant shift s is then found by averaging s_N , weighted by the statistical error σ_{s_N} :

$$s = \frac{\sum_N s_N \sigma_{s_N}^{-2}}{\sum_N \sigma_{s_N}^{-2}}. \quad (4.4)$$

The fixed shifts found this way are given in Table 4.1. The largest shift is found for the combinatorial

ensemble, the smallest shift is found for the maximally degenerate ensemble, close to 0. Now, the distributions $k_N^{-1} \rho_N^{\mathcal{T}}(k_N^{-1}(x+s) - s)$ can be fitted to $\rho_{N_0}^{\mathcal{T}}(x)$. The rescaled curves obtained from this fit are presented in Fig. 4.2. Note that generally, a collapse of the curves is achieved, confirming the assumption of (4.2). The collapse of the curves measured in the combinatorial ensemble shows visible imperfections around the peak of the curves, which are less prominent in the curve collapse of the degenerate ensembles.

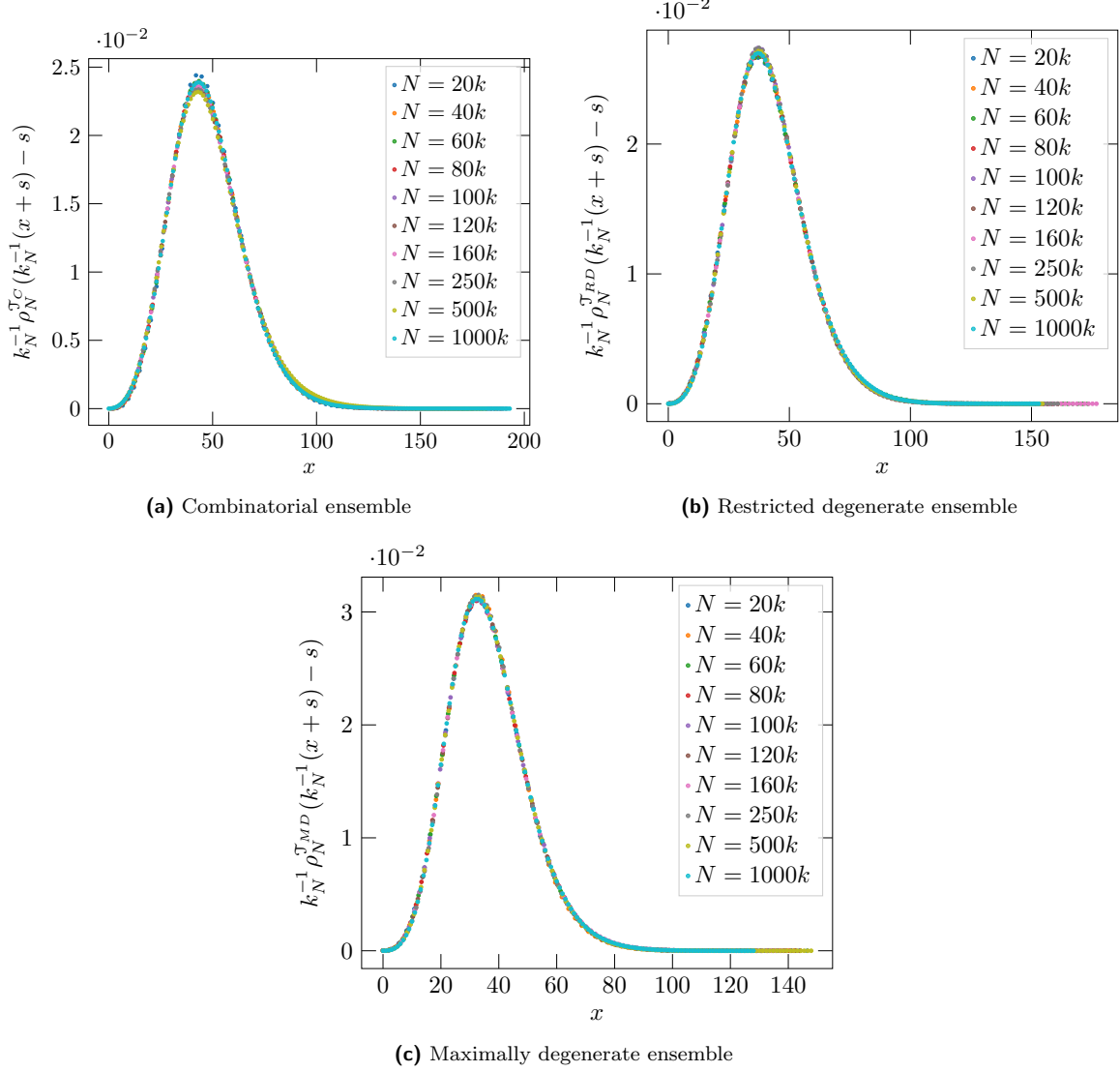


Figure 4.2: Collapse of the curves $k_N^{-1} \rho_N^{\mathcal{T}}(k_N^{-1}(x+s) - s)$ to $\rho_{N_0}^{\mathcal{T}}(x)$, with $N_0 = 1000k$, shown for all three ensembles.

Table 4.1: Fixed shifts found for the three ensembles.

Ensemble	s
\mathcal{T}_C	2.330 85
\mathcal{T}_{RD}	0.443 18
\mathcal{T}_{MD}	0.006 80

Using (4.2), the scaling factors k_N should follow

$$\frac{k_N}{k_{N_0}} = c \left(\frac{N}{N_0} \right)^{-1/d_H} \quad (4.5)$$

in the large N limit, with $c \approx 1$. Since the scaling factors have been obtained for all N considered, an estimate for d_H can be found by fitting (4.5) to the data. This is performed for all three ensembles. The scaling factors k_N , as well as the aforementioned fits, are presented in Fig. 4.3. The corresponding estimates for d_H are presented in Table 4.2. Note that by fitting equation (4.5) to the data, our approach deviates from that of [11], where a subleading term is included in the fit function. The reason for this difference in approach is discussed in more detail in section 4.3.

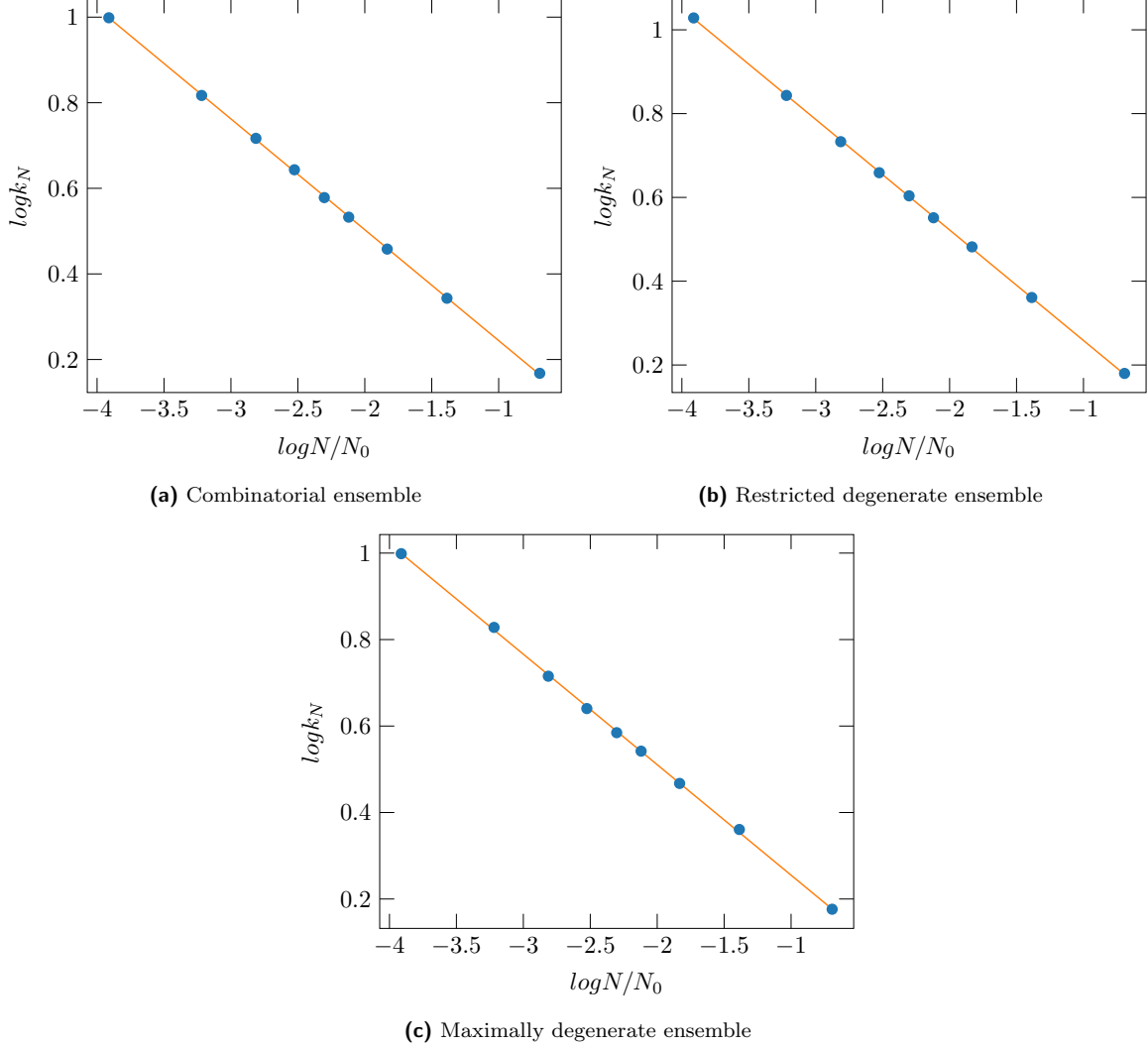


Figure 4.3: Log-log plot of the scaling factors k_N as a function of the triangulation size N , relative to the reference size of $N_0 = 10^6$, for all three ensembles. Linear fits are presented in orange. Error bars are smaller than the dot size.

4.3 Discussion

The estimates for the Hausdorff dimension of Table 4.2 are close to the expected value of $d_H = 4$, especially the estimate for the maximally degenerate ensemble. However, they do not agree with the expected value of 4 within error bars. Finite-size effects could play a role in this discrepancy. In [35], where maximally degenerate triangulations are studied, the authors find an estimate for the Hausdorff dimension $d_H \approx 3.8$, and show how it depends on the triangulation sizes considered. Specifically, the estimate for the Hausdorff dimension is closer to 4 if only larger sizes are considered. It must be noted that the triangulation sizes used in [35], with a maximum of $N = 32k$, are significantly smaller than those used in the present work, with a maximum of $N = 1000k$. Indeed, it appears that by performing measurements at larger N we have found a better estimate for the Hausdorff dimension for the maximally degenerate triangulations, namely $d_H = 3.914 \pm 0.013$.

Table 4.2: Hausdorff dimensions found from curve collapse. Specifically, these results are obtained from the power law fits of Fig. 4.3 for the three ensembles.

Ensemble	d_H
\mathcal{T}_C	3.880 ± 0.010
\mathcal{T}_{RD}	3.798 ± 0.011
\mathcal{T}_{MD}	3.914 ± 0.013

The fitting performed to obtain the values presented in Table 4.2 does not follow the procedure given in [11]. Instead of fitting to eq. (4.5), the fitting function used in [11] contains a subleading term:

$$k_N = \left(\frac{N}{N_0}\right)^{-1/d_H} \left(a + b \left(\frac{N}{N_0}\right)^{-\delta}\right), \quad (4.6)$$

with $a \approx 1$, $b \approx 0$, and $\delta > 0$. However, this prescription proves difficult to apply to the present data. The fit results, especially the parameters b and δ , do not stay within reasonable bounds. Moreover, we checked that these results are not robust under resampling of the data when bootstrapping, which is the method used for error estimation. The number and range of triangulation sizes considered in the present work is likely too small to reliably fit to eq. (4.6), with its four free parameters. The present data only considers nine triangulation sizes, ranging from $20k$ to $1000k$ triangles, whereas the authors of [11] consider 15 different quadrangulation sizes, ranging from 2^8 to 2^{24} squares. Additionally, better statistics could help make the result for b and δ more robust under resampling.

In [35], the authors present a different method of estimating d_H from the distributions $\rho_N^{\mathcal{T}}(r)$. From eq. 4.2, the location r_0 of the peak, and the corresponding maximum value $\rho_N^{\mathcal{T}}(r_0)$ are expected to scale as

$$r_0 \propto N^{1/d_H}, \quad (4.7)$$

$$\rho_N^{\mathcal{T}}(r_0) \propto N^{-1/d_H}, \quad (4.8)$$

respectively. The peak location is determined by fitting $\rho_N^{\mathcal{T}}(r)$ to

$$\rho_N^{\mathcal{T}}(r) = P_4(r) \exp(-ar^b), \quad (4.9)$$

where $P_4(r)$ is a fourth-order polynomial in r . The maximum is then determined using the fitted function. The locations and heights of these maxima can then be fitted to (4.7) and (4.8) respectively. This prescription is performed here for all three ensembles and the results are presented in Table 4.3.

Table 4.3: Estimates for the Hausdorff dimension in the three ensembles. The column denoted by “location” contains the results obtained from scaling of $\rho_N^{\mathcal{T}}$ peak location, the column denoted by “height” contains the results obtained from scaling of $\rho_N^{\mathcal{T}}$ peak height.

Ensemble	d_H	
	from location	from height
\mathcal{T}_C	3.625 ± 0.011	3.677 ± 0.018
\mathcal{T}_{RD}	3.767 ± 0.014	3.869 ± 0.018
\mathcal{T}_{MD}	3.930 ± 0.015	3.922 ± 0.017

They again exhibit deviations from $d_H = 4$ which rapidly shrink when going to more degenerate ensembles. However, even for the maximally degenerate ensemble, neither the results for d_H obtained from peak height, nor from peak location fall within error bars of $d_H = 4$. The authors of [35] have demonstrated that local restrictions on the sphere growth can have a large influence on the estimate for the Hausdorff dimension, by comparing curve collapse for measurements on the direct lattice to those on the dual lattice, where they find $d_H = 3.790 \pm 0.030$ and $d_H = 3.150 \pm 0.031$ respectively. They find similar discrepancies between the direct and dual lattice when obtaining estimates for the Hausdorff dimension from the scaling of peak height and location. These discrepancies are explained as follows. In the dual lattice, the degree of all vertices is 3, which implies an upper bound for the ball boundary length as a function of r . This upper bound pushes the power law scaling one expects from the sphere

growth out to larger radii, which in turn could lead to finite-size effects in triangulations that are not sufficiently large for these larger radii to be available. This argument is not directly applicable here, since none of our ensembles have upper bounds on the vertex degree. Nonetheless, the restricted degenerate and combinatorial ensembles come with local gluing restrictions, compared to the maximally degenerate ensemble. Perhaps these restrictions similarly restrict the ball boundary length growth at small radii. However, further investigation is needed to confirm this.

Chapter 5

Average Sphere Distance

This chapter presents the measurements of the average sphere distance, defined in section 2.4.1. Section 5.1 presents the methods used. The results of measurements in the combinatorial ensemble are presented in 5.2. The results of measurements in the degenerate ensembles are presented in 5.3. A discussion of the results is given in section 5.4. This section also contains improvements on the presented method, with their corresponding results. Finally, section 5.5 presents a summary of these improvements.

5.1 Methods

The methodology for measuring the average sphere distance in 2D EDT follows that of [7] closely. It is reiterated here for completeness, but also to make clarifications, or expand upon it. In the following, whenever a deviation from the approach in [7] is present, it is indicated.

As stated in section 2.4, the quantity of interest is the expectation value of an observable. Here, the observable of interest is the average sphere distance $d_T(\delta)$, as defined in (2.22), for a given ensemble $\mathcal{T} \ni T$. Using the MCMC algorithm outlined in section 2.5, \mathcal{T} can be sampled uniformly, and an estimate of $\langle d_T(\delta) \rangle_{\mathcal{T}}$ is obtained as the sample mean. Denote the expectation value of $d_T(\delta)$ for an ensemble \mathcal{T} at fixed size N as $\langle d_T(\delta) \rangle_N$. Then, the quantity approximated in the simulations is

$$\frac{\bar{d}_N(\delta)}{\delta} = \frac{\langle d_T(\delta) \rangle_N}{\delta}. \quad (5.1)$$

To this end, the following measurements are made. For each sample triangulation T , pick a point p uniformly at random from its set of vertices $V(T)$. This point p is kept fixed during the following steps. For each $\delta = 1, \dots, \delta_{max}$, a point p' is picked uniformly at random from S_p^δ , and the average sphere distance $\bar{d}(S_p^\delta, S_{p'}^\delta)$ is calculated, as introduced in section 2.4.1. Similar to [7], δ_{max} is set to 15 for now. In total, these measurements are performed on 2×10^4 sample triangulations of sizes $N = 20, 30, 40, 60, 80, 120, 160$, and $240k$, and for the ensembles \mathcal{T}_C , \mathcal{T}_{RD} , and \mathcal{T}_{MD} . Between each sample triangulation a sufficient number of updates is performed, in accordance with the conclusions of section 3.3. The number of measurements for $N = 20$ and $30k$ is lower than in [7], since at 2×10^4 the statistical error is deemed to be sufficiently small already. Furthermore, the methodology of the present work differs from that of [7] by performing measurements in the degenerate ensembles.

Note that the prescription above takes shortcuts to save on computation time. Generating a new triangulation sample T is much less time-consuming than performing all the average sphere distance measurements needed for $\bar{d}_T(\delta)$, defined in (2.22). Instead of calculating an average sphere distance for every δ -separated point pair, only one point pair is considered for each distance δ , in each triangulation T . Furthermore, for a given triangulation T , the point pairs at the different distances δ all contain the point p . This way, different average sphere distance measurements at a given δ never consider overlapping area's, thus avoiding correlation. Additionally, keeping p fixed in constructing the point pair for each δ allows one to construct $S_p^{\delta+1}$ from S_p^δ .

As pointed out in [9], the aforementioned prescription for sampling the point pair p, p' introduces a bias, particularly for small δ . In approximating the sum over all δ -separated point pairs of T in equation (2.22) by only considering one point pair, one would ideally sample this point pair uniformly, that is, as if picked blindly from a list of all δ -separated point pairs of T . The construction outlined does *not* provide a uniform point pair sampling in this sense. Instead, the probability of picking a given point pair in

this way is dependent on the sphere sizes $|S_p^\delta|$ and $|S_{p'}^\delta|$, which may be correlated to the average sphere distance. The effect of this sampling bias on vertex degree two-point functions has been studied in 2D CDT [9]. The biased sampling resulted in a statistically significant deviation from the results obtained with uniform sampling, but only for lower distances. For this reason, we assume that this sampling bias is a small- δ effect and will not affect continuum results, and the biased point pair selection laid out above is still used. Furthermore, it replicates the methodology of [7], which is used as a starting point for incremental improvement.

To make a comparison of curvature profiles of 2D EDT and of continuum spheres, one must resolve the matter of determining c_{av} on piecewise flat manifolds. As mentioned in section 2.4.1, evaluating $c_{av} = \lim_{\delta \rightarrow 0} \bar{d}_T(\delta)/\delta$ is not a meaningful prescription on the lattice. Following [7], c_{av} is determined by demanding the curves go through a common point at a δ_{discr} at which the discretization effects are deemed sufficiently small. To start with, δ_{discr} is set to 5, matching the choice made in [7].

5.2 Results for combinatorial triangulations

First, the measurements for the combinatorial ensemble \mathcal{T}_C are presented. These replicate the methodology of [7], and illustrate the analysis used to come to their conclusion. Figure 5.1 shows the curvature profile for combinatorial triangulations of size $N = 40k$. Additionally, the best fit of the 4-sphere curvature profile is included. After setting both curves equal at $\delta = \delta_{discr}$ by introducing a vertical shift, the only fit parameter is the curvature radius ρ . Note that only data points with $\delta > \delta_{discr}$ are included in the fit. The best fit curvature radius $\rho_{eff} = 16.67$ is found. This fit procedure is then repeated for all combinations of dimensions D of the sphere curvature profiles and triangulation sizes N .

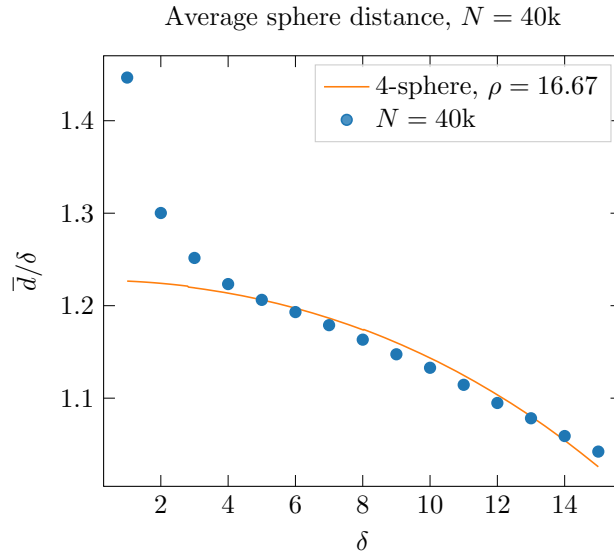


Figure 5.1: The curvature profile for combinatorial triangulations of size $N = 40k$, in blue. Error bars are smaller than marker size. A fit of the 4-sphere curvature profile is pictured, in orange. The radius obtained from this fit is $\rho = 16.67$.

In [7], the authors concluded that the fit quality was not sufficient to decide for which D the sphere curvature profiles resemble that of 2D EDT best. To resolve this issue, they invoked the following additional argument. A \mathcal{D} -sphere's¹ volume scales with its radius ρ in the following way:

$$V \propto \rho^{\mathcal{D}}. \quad (5.2)$$

The fitting results of the fit shown in Fig. 5.1 and likewise for the other triangulation sizes and sphere dimensions, provide a ρ_{eff} for every triangulation size N , and for each D . Using these, for each value of D , one can determine the best-fit volume-radius scaling dimension \mathcal{D} , since N is proportional to V . Then, a self-consistency argument is employed. That is, the sphere dimension D that describes the curvature properties of 2D EDT best is that where D and \mathcal{D} agree. In Fig. 5.2 the (N, ρ_{eff}) data points are presented for $D = 4$, along with a power law fit through them. Here, \mathcal{D} is found to be 5.30 ± 0.11 .

¹Note the calligraphic font that is used here. Crucially, this \mathcal{D} is not necessarily equal to D . Although this notation may cause confusion, it is used to be consistent with [7].

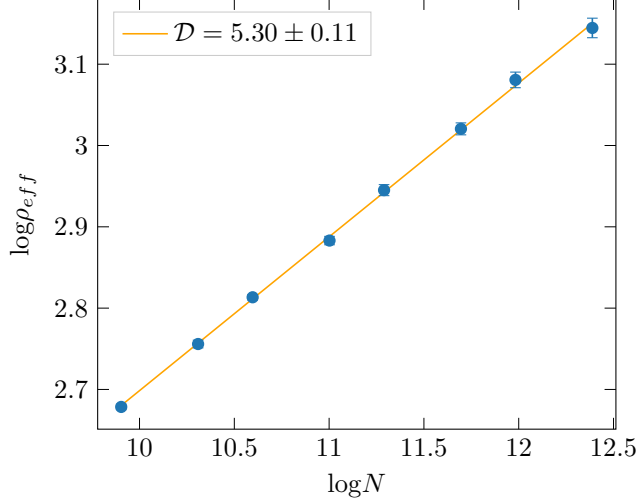


Figure 5.2: Example of a log-log plot of the effective curvature radii ρ_{eff} as function of triangulation size N , for combinatorial triangulations, shown in blue. (Error bars are smaller than the dot size.) The values shown here are obtained from fits to $D = 4$ -sphere curvature profiles. A linear fit is made, shown in orange. The power law exponent $\mathcal{D} = 5.30 \pm 0.11$ is found.

Repeating for the other values of D gives the results shown in Table 5.1. The results found in [7] are also included. The present results are systematically larger than those found in [7], with (mostly) non-overlapping error bars. Possible causes of this discrepancy are discussed in section 5.4.1. Despite this discrepancy, the same conclusion is still drawn: \mathcal{D} and D match best at $D = 5$.

Table 5.1: Values of \mathcal{D} found for a range of sphere dimensions D , based on average sphere distance measurements in the combinatorial ensemble \mathcal{T}_C . The values in the “Present results” column are based on measurements performed for the present work. Values in the last column are taken from [7]

D	\mathcal{D}	
	Present results	Results from [7]
2	6.00 ± 0.14	5.7 ± 0.3
3	5.38 ± 0.12	5.02 ± 0.17
4	5.30 ± 0.11	4.92 ± 0.17
5	5.15 ± 0.11	4.85 ± 0.16

5.3 Results for degenerate triangulations

The curvature profiles measured for the degenerate ensembles \mathcal{T}_{RD} and \mathcal{T}_{MD} are also compared to those of smooth D -spheres. Again, fits are made, and for both ensembles the resulting ρ_{eff} values are shown as a function of triangle number N , for $D = 4$, in Fig. 5.3, as well as a power law fit. For both degenerate ensembles the values for \mathcal{D} found for the various sphere dimensions D are shown in Table 5.2. The values for \mathcal{D} in Table 5.2 lie slightly lower than those found for the combinatorial ensemble shown in Table 5.1, more so for the restricted degenerate ensemble. Similar to the results for the combinatorial ensemble, \mathcal{D} decreases with increasing D . The conclusion that was found for the combinatorial ensemble is found for both the degenerate ensembles as well: \mathcal{D} and D match best at $D = 5$.

Based on these results, and those presented in section 5.2, one may be tempted to consider the conclusion of [7] to be confirmed. However, as mentioned in section 5.2, the combinatorial ensemble result show a discrepancy with the results in [7] that warrants further investigation. Furthermore, one must be careful not to take the results of the present section at face value. Despite the apparent good quality of the fit in Fig. 5.2, Figures 5.3a and 5.3b show that for the other two ensembles, for $D = 4$, a power law is not a good fit for the data. The same holds when considering other values of D for the degenerate ensembles. In the log-log plots, the slope is lower for (roughly) the smallest three triangulation

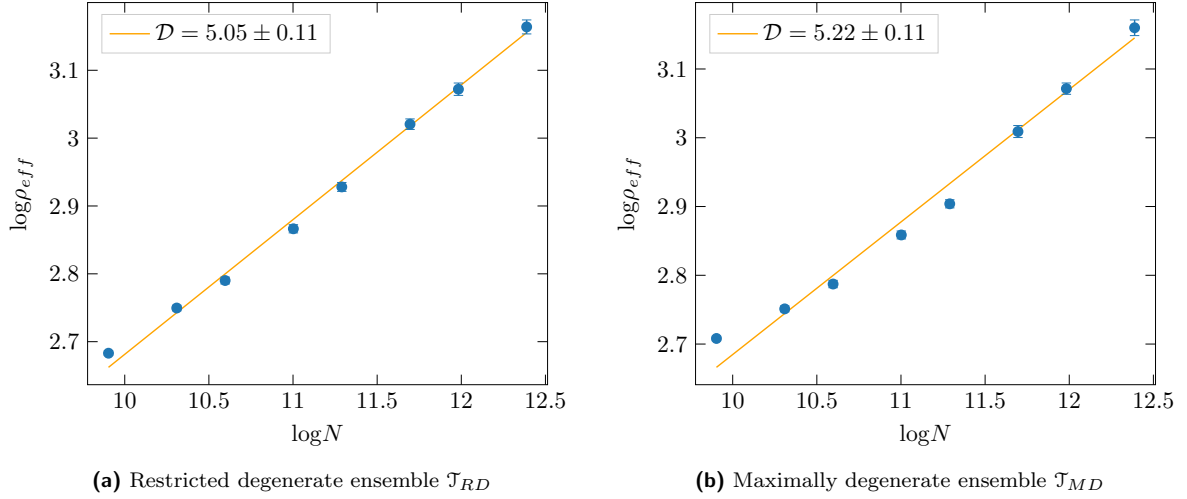


Figure 5.3: Examples of log-log plots of the effective curvature radii ρ_{eff} as function of triangulation size N , for restricted degenerate triangulations (a) and maximally degenerate triangulations (b). (Error bars are smaller than the dot size in both.) The values shown here are obtained from fits to $D = 4$ -sphere curvature profiles. A linear fit is made for both, shown in orange. The resulting power law exponent \mathcal{D} has been added.

Table 5.2: Values of \mathcal{D} found for a range of sphere dimensions D . The \mathcal{T}_{RD} column represents the values found for the restricted degenerate ensemble, the \mathcal{T}_{MD} column represents the values found for the maximally degenerate ensemble.

D	\mathcal{D}	
	\mathcal{T}_{RD}	\mathcal{T}_{MD}
2	5.76 ± 0.13	5.97 ± 0.14
3	5.14 ± 0.11	5.31 ± 0.12
4	5.05 ± 0.11	5.22 ± 0.11
5	4.91 ± 0.10	5.07 ± 0.12

sizes. Finite-size effects could be a possible explanation. Alerted by these findings, investigations into the effects of discretization and finite-size effects are presented in sections 5.4.2 and 5.4.3, respectively

5.4 Discussion

5.4.1 Discrepancy with previous work

The results obtained for the combinatorial ensemble show discrepancies from previous work. A comparison is presented in Table 5.1. Since the data and programs used in [7] were no longer available, rigorous checks can only be performed on the present experimental results and methodologies. Three potential causes for the discrepancy are identified:

- (i) statistical error,
- (ii) different triangulation generation, and
- (iii) different average sphere distance measurement implementation.

(i) The values in the two columns of Table 5.1 are all at least one standard deviation apart from each other at equal D . The fact that these statistical errors are relatively small compared to the difference in the actual results suggests the presence of a systematic difference between the present methods, and those used in [7]. However, at a difference of two to three error bars one cannot definitively dismiss statistical error as a cause. On the contrary, the curvature profile itself, specifically the value at $\delta = 1$, *does* provide a definitive discrepancy. Visual inspection of Fig. 4 in [7] gives $\bar{d}/\delta|_{\delta=1} = 1.59 \pm 0.01$, where the error bar is determined by the scale reading uncertainty, due to the obscured error bars in the figure. Using the same settings ($N = 40k$, $D = 4$, $\mathcal{T} = \mathcal{T}_C$), the present experiments find $\bar{d}/\delta|_{\delta=1} = 1.447 \pm 0.002$.

Even when considering the read-off uncertainty, which is an upper bound, as the statistical uncertainty σ , these values differ by at least 14σ . This discrepancy leaves no doubt that a difference in methodology is present. The found discrepancy is largest for small δ .

(ii) If the triangulation generation is faulty, one would of course expect different outcomes even when all other parts of the algorithm are implemented correctly. Unfortunately, there is no check that guarantees the triangulations generated are correctly distributed. However, the vertex degree distribution measurements provide an estimation, since for \mathcal{T}_C the theoretical distribution is readily available. However, it should be noted that agreement of the vertex degree distribution is only a necessary, and not a sufficient condition. Considering the measurements presented in Fig. 3.2a, the measured distribution matches the theoretical prediction perfectly. Furthermore, our measurements of the Hausdorff dimension presented in section 2.5 show agreement with theoretical predictions, as well as the wealth of existing experimental data. Based on these agreements, the triangulations are deemed to be distributed as expected.

(iii) A mistake could also have been made in the implementation of the average sphere distance measurement algorithm. As a check of the present implementation, a new implementation was created using the Python programming language. Generated triangulations are imported, and the Networkx [36] package is used for the graph exploration that is necessary when determining the average sphere distance. Moving this part of the implementation to a well-tested package removes most of the room for error. A drawback is that this implementation is relatively slow. Therefore, it is only suitable for evaluating the average sphere distance for small δ . The results are shown in Table 5.3. All results fall within each other's error bars. It follows that the present implementation is likely free of significant errors.

Table 5.3: Values of \bar{d}/δ found for a range of radii δ . The “C++” column represents the values found using the initial C++ implementation, the “Python” column represents the values found using the Python implementation. The results in this column are based on 5000 measurements, except for (*), which is based on 300 measurements.

δ	\bar{d}/δ	
	C++	Python
1	1.4473 ± 0.0024	1.4502 ± 0.0048
2	1.3014 ± 0.0019	1.3001 ± 0.0038
3	1.2535 ± 0.0017	1.2489 ± 0.0034
4	1.2296 ± 0.0016	1.2416 ± 0.0139 *

A possible difference between the present analysis and that of [7] is the treatment of the case where $d(q, q') = 0$, which may arise when calculating the average sphere distance (see Fig. 2.8). To elaborate on this, let us first present the details of the algorithm used to calculate the average sphere distance between the spheres S_p^δ and $S_{p'}^\delta$. Recall that the average sphere distance is given by equation (2.19). Adapted to triangulations, and setting $\epsilon = \delta$, it reads:

$$\bar{d}(S_p^\delta, S_{p'}^\delta) = \frac{1}{|S_p^\delta|} \frac{1}{|S_{p'}^\delta|} \sum_{q \in S_p^\delta} \sum_{q' \in S_{p'}^\delta} d(q, q'). \quad (5.3)$$

In the present implementation, the distance between q and q' is found using a breadth-first search (BFS), that is, by constructing a sphere of radius one around q , and repeatedly increasing its radius by one until q' is found. Then, the distance between q and q' is given by the radius of the sphere at the end of this process. Instead of performing a BFS for each pair of q and q' , the distance of q to every point q' in $S_{p'}^\delta$ is determined in a single breadth-first search. Instead of growing the sphere until one desired point q' is found, the sphere is grown until all points of $S_{p'}^\delta$ have been encountered. This altered BFS is performed for each point q in S_p^δ , recording all the distances to the points encountered in a single list. The average sphere distance is then simply the mean of this list of distances, but only if one records a distance $d(q, q') = 0$ in the case q is a vertex in both S_p^δ and $S_{p'}^\delta$. If not, the mean of the list of distances does not correspond to eq. (5.3). The sum of distances is still equal, however the normalization factor may not be. The inclusion of these distances of 0 is easy to miss² by starting the breadth first search at a radius of one, instead of zero. To estimate the effect of this normalization error, an intentionally faulty average sphere distance implementation is made. At $\delta = 1$, this faulty implementation finds

²The claim that this mistake is easy to make comes from first-hand experience. The initial analysis did contain this error, but the results that are presently presented do not.

$\bar{d}/\delta = 1.5454 \pm 0.0043$. This difference lies approximately 5σ from the results found in [7], as opposed to the 14σ difference that was present before. Furthermore, the effect of this normalization difference is expected to decrease with growing δ . Qualitatively, this behavior follows the discrepancy between the present results and those presented in [7], which are also largest at small δ .

In conclusion, neither statistical error nor differences in the triangulation generation and average sphere distance measurement implementation can fully explain the discrepancy. A difference in normalization for the average sphere distance may play a role. Qualitatively, the effect of the different normalization matches the discrepancy to the results of [7]. However, even after compensating for this effect, a statistically significant discrepancy remains. Due to the one-sided nature of this comparison of methodologies, no definitive cause can be pinpointed for the discrepancy. Despite leaving this question open, this a posteriori investigation into the measurements of section 5.2 does provide confidence in the validity of these measurements, and the analyses that follow.

5.4.2 Discretization effects

Discretization effects may play a role for small distances δ . The fit curve presented in Fig. 5.1, which is fitted to the data points with $\delta \geq 5$, is far from perfect. For any size of triangulation, the curvature profile has roughly the same shape: it starts with a steeply dropping concave up³ part, followed by a slightly concave down tail. The initial concave up part is considered to be caused by discretization effects [5]. The value $\delta_{discr} = 5$ appears to be a low estimate for the end of this region. Recall that for the fit to the D -sphere curvature profiles, a vertical offset is fixed by letting the curves coincide at $\delta = \delta_{discr}$. Therefore, the resulting ρ_{eff} that is obtained from this fit is expected to be sensitive to any discretization effects that are present at δ_{discr} . To make a more quantitative argument for what a good value of δ_{discr} would be, the aforementioned transition from concave up to concave down of the EDT curvature profiles is examined. To this end, the discrete second derivative⁴ of the curvature profiles is determined. For \mathcal{T}_C , and for all sizes for which the curvature profile is measured, the second derivative of the curvature profile is shown in Fig. 5.4. At $\delta = 5$, the majority of the curves are still concave up, especially for the larger sizes. A higher value of δ_{discr} is therefore deemed better. However, increasing δ_{discr} has its own drawbacks. Only the data points for $\delta \geq \delta_{discr}$ are taken into account, and consequently raising δ_{discr} means discarding data. Based on this trade-off, $\delta_{discr} = 7$ is deemed to be the best choice for \mathcal{T}_C . Note that discrete derivatives are very susceptible to noise, and $\partial_\delta^2 (\bar{d}/\delta) < 0$ is not a very rigorous criterion to identify the discretization radius. However, it is still the preferable approach, considering the alternative is visual inspection.

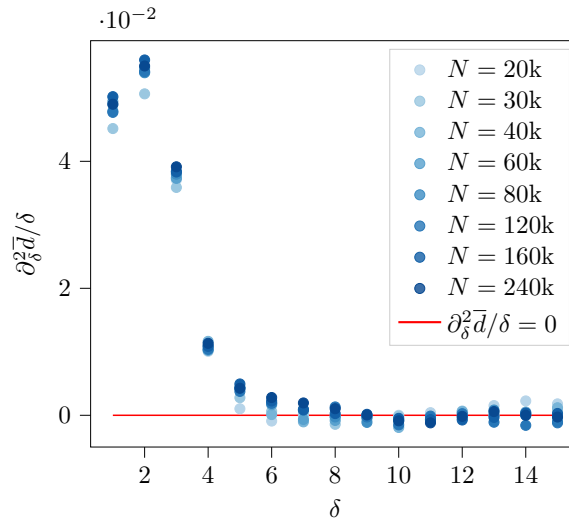


Figure 5.4: Discrete second derivative of the curvature profile for triangulation sizes N ranging from $20k$ to $240k$, for the combinatorial ensemble. In red, the horizontal line $\partial_\delta^2 (\bar{d}/\delta) = 0$ is added. For clarity, error bars are not shown. The error bars range from 0.001 to 0.005 .

Similar analyses are performed for the degenerate ensembles. The second derivatives of the curvature profiles are shown in Fig. 5.5. For \mathcal{T}_{RD} and \mathcal{T}_{MD} , $\delta_{discr} = 6$ is deemed sufficiently large.

³Here concave up(down) refers to the shape of the graph of a function whose second derivative is positive(negative).

⁴The discrete second derivative is obtained by two consecutive applications of the *numpy.gradient* NumPy [37] method.

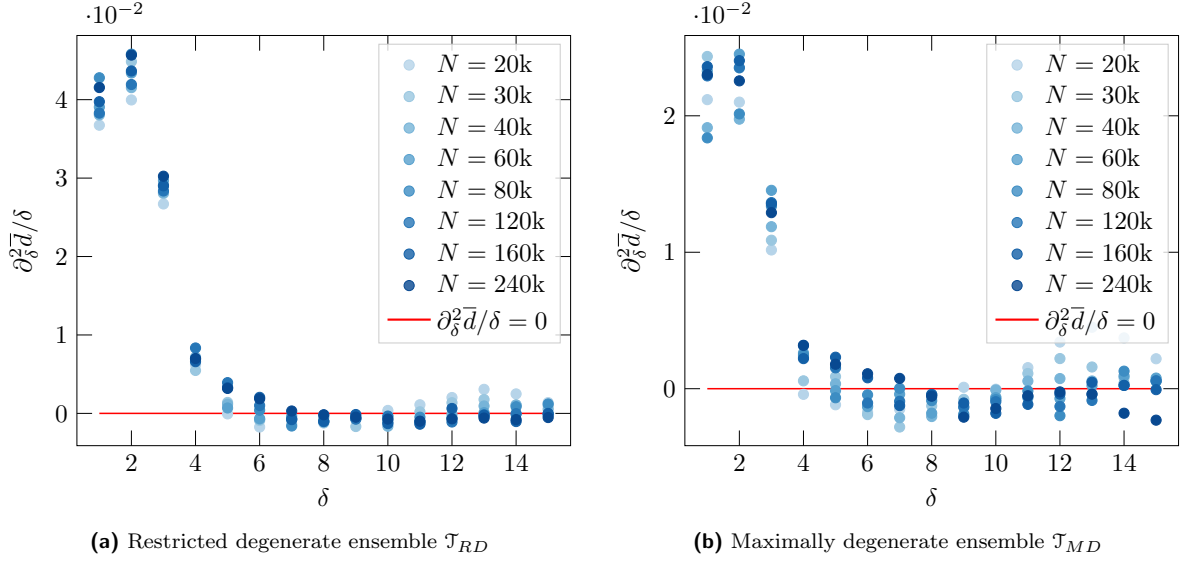


Figure 5.5: Discrete second derivatives of the curvature profile for triangulation sizes N ranging from $20k$ to $240k$, for the restricted degenerate ensemble (a) and the maximally degenerate ensemble (b). In red, the horizontal line $\partial_\delta^2 (\bar{d}/\delta) = 0$ is added in both. For clarity, error bars are not shown. The error bars range from 0.001 to 0.005 .

This new choice of δ_{discr} changes the values of ρ_{eff} that are found from the fits to the sphere curvature profiles, for all three ensembles. Of particular interest are the changes for the combinatorial ensemble, where a qualitative difference is found compared to the results for $\delta_{discr} = 5$. Previously, the plot of $\log(\rho_{eff})$ as a function of $\log(N)$ had shown a near perfect straight line (see Fig. 5.2). Now, with δ_{discr} set to 7 , the shape is similar to that of the degenerate ensembles: a lower slope for smaller values of N . This can be seen in Fig. 5.6. As a result, the values for \mathcal{D} found from a power law fit are significantly lower. For example, for $D = 4$, we find $\mathcal{D} = 4.68 \pm 0.12$, in contrast to the result $\mathcal{D} = 5.30 \pm 0.11$ found before, shown in Figure 5.2. Again, this lower slope for the smaller values of N is an indication of finite-size effects, which are discussed in more detail in section 5.4.3.

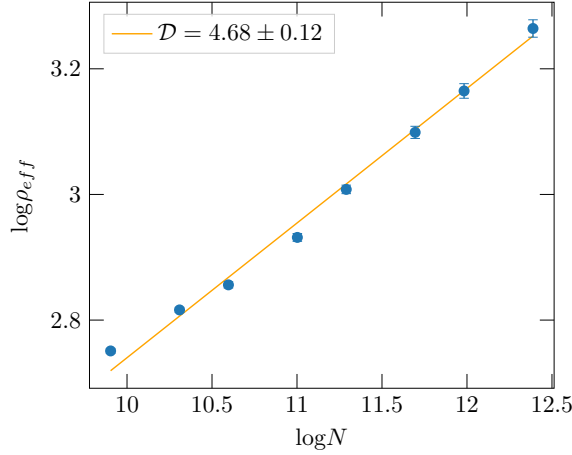


Figure 5.6: Log-log plot of the effective curvature radii ρ_{eff} as function of triangulation size N , for combinatorial triangulations and with $\delta_{discr} = 7$, shown in blue. These are obtained from fits to $D = 4$ -sphere curvature profiles. A linear fit is made to all data points, shown in orange. The resulting power law exponent $\mathcal{D} = 4.68 \pm 0.12$ is found.

5.4.3 Finite-size effects

After the adjustments of δ_{discr} in the previous section, the log-log plots of Figures 5.3 and 5.6, which show ρ_{eff} as a function of N show the following behavior: a near perfect straight line for the larger values of N , roughly $N \geq 60k$, with a decreasing slope near the lower values of N , roughly $N < 60k$.

This deviation from the expected power-law behavior at low N suggests that finite-size effects play a role at small volumes. Consider the distances involved in a measurement of $\bar{d}(S_p^\delta, S_{p'}^\delta)$. The pairs of points q, q' can be at most a distance 3δ apart. With $\delta_{max} = 15$, the longest possible distance between q and q' is 45. At this scale, the triangulations do not resemble round spheres. For instance, consider the sphere area measurements performed to determine d_H , presented in Fig. 4.1. Past their peak, these curves do not resemble the shape one would expect for a 4-sphere [7]. Note that $\delta = 45$ is well past the peak for the sizes considered in the average sphere distance measurements. This does not mean all data should necessarily be discarded, the value of $3\delta_{max}$ is only an upper bound after all. Still, it illustrates that the average sphere distance measurements probe length scales at which the triangulations do not resemble smooth spheres, especially for the smaller triangulation sizes.

First, a crude method of avoiding these finite-size effects is presented. The effective radii for the sizes $N = 20, 30$, and $40k$ are simply not incorporated in the $N \propto \rho_{eff}^{1/D}$ power law fit. The resulting fits for all three ensembles, and $D = 4$, are presented in Fig. 5.7. In these figures the fit function is shown for the whole range of triangulation sizes N . The graph is dashed for $N \leq 40k$, to indicate these points are not incorporated in the fit. The figures clearly show the lower slope for the lower triangulation sizes. The full set of results for the various values of D are presented in Table 5.4. For all three ensembles, \mathcal{D} and D agree best at $D = 4$. This approach may be wasteful, in the sense that measurements for relatively low δ are omitted for the lower sizes, even though at these shorter length scales measurements may not be subject to significant finite-size effects.

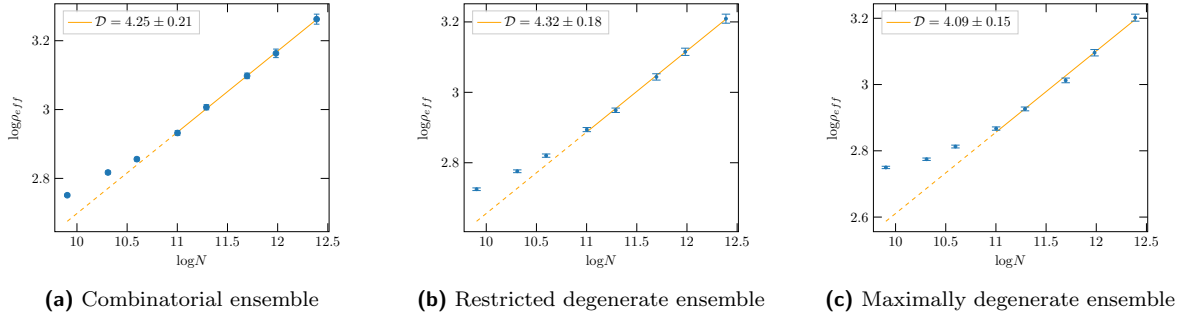


Figure 5.7: Log-log plot of the effective curvature radii ρ_{eff} as function of triangulation size N for all three ensembles. A linear fit is made, shown in orange. This fit is not made to all data points, but only to the data points corresponding to the sizes $N \geq 60k$, located at the transition of dashed to solid in the figure. The resulting power law exponents are presented in the legends. The values shown are obtained from fits to $D = 4$ -sphere curvature profiles. For combinatorial triangulations, δ_{discr} is set to 7 (a). For the restricted (b) and maximally (c) ensembles, δ_{discr} is set to 6.

Table 5.4: Values of \mathcal{D} found for a range of sphere dimensions D . Triangulation sizes $N \leq 40k$ have been excluded from the power law fits, as opposed to the values shown in Tables 5.1 and 5.2, where the full range of sizes was used in the fits. The \mathcal{T}_C , \mathcal{T}_{RD} , and \mathcal{T}_{MD} columns represent the results for the combinatorial, restricted degenerate, and maximally degenerate ensembles. In obtaining these results, δ_{discr} is set to 7, 6, and 6 respectively.

D	\mathcal{D}		
	\mathcal{T}_C	\mathcal{T}_{RD}	\mathcal{T}_{MD}
2	4.54 ± 0.22	4.66 ± 0.20	4.44 ± 0.17
3	4.29 ± 0.21	4.36 ± 0.17	4.12 ± 0.15
4	4.24 ± 0.21	4.31 ± 0.18	4.10 ± 0.15
5	4.21 ± 0.22	4.24 ± 0.19	4.02 ± 0.16

In an attempt to discard fewer data points, a more careful approach is also used. Instead of omitting all data for the triangulation sizes $N = 20, 30$, and $40k$, only the data points gathered for values of δ that are sufficiently sensitive to finite-size effects are discarded. Of course, it is difficult to judge this exactly. However, it is possible to make an estimate based on the following argument. Assume the maximum δ for which finite-size effects are found is proportional to the location of the peak of the sphere area curves of Fig. 4.1. According to [35], and corroborated by the measurements of chapter 4, the location of these peaks follows a power-law scaling as a function of triangulation size, with scaling dimension equal to the

Hausdorff dimension. One then only needs to pick a reference size N_{ref} , for which the measurements at δ_{max} are still sufficiently free of finite-size effects. Then, the δ_{max} values for $N \leq N_{ref}$ are found using

$$\delta_{max}(N) = 15 \cdot \left(\frac{N}{N_{ref}} \right)^{1/d_H}. \quad (5.4)$$

Of course, δ_{max} is not a continuous variable, so rounding is applied where necessary. For all ensembles, $N_{ref} = 80k$ is chosen based on visual inspection. After rounding, the δ_{max} values that follow for the triangulations with sizes $N < N_{ref}$ are 11, 12, 13, and 14.

Recall that in section 5.4.2, δ_{discr} was chosen to be 7, 6, and 6 for the combinatorial and both degenerate ensembles respectively. Combined with the δ_{max} values found in the present section, the following results are found. Power law fits for ρ_{eff} as a function of N , for $D = 4$ and all three ensembles, are presented in Fig. 5.8. Note how the scaling δ_{max} has removed the finite-size effects, which could be seen in Fig. 5.7: in the log-log plots, all data points appear to lie on a single line. Results for all values of D are presented in Table 5.5. Note that the error on these results is now roughly halved compared to the “wasteful” method presented in the previous section. Furthermore, at $D = 4$, the values of \mathcal{D} agree with 4 to within one error bar, for \mathcal{T}_C and \mathcal{T}_{RD} . The value of \mathcal{D} at $D = 4$ found for \mathcal{T}_{MD} is just barely more than one error bar away from 4. The quality of this agreement leads us to conclude that the curvature of 2D EDT resembles that of a sphere of dimension four. This conclusion is contrary to that of [7], finding resemblance to a sphere of dimension five.

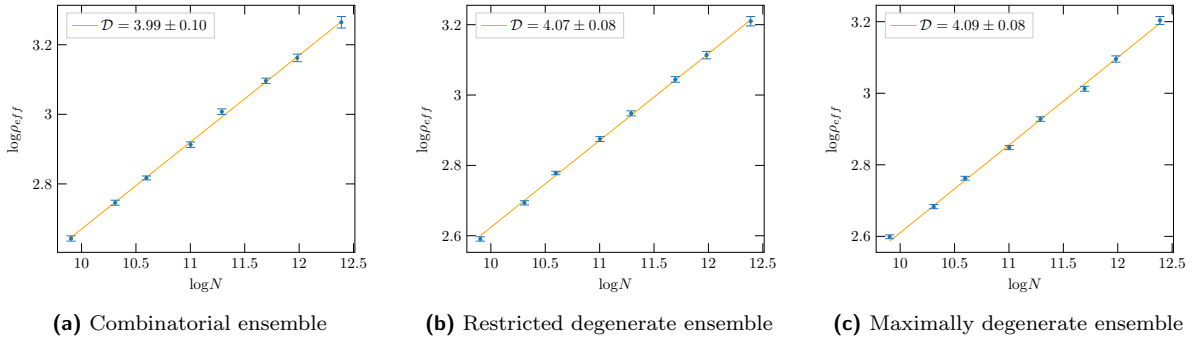


Figure 5.8: An example for $D = 4$, of log-log plots of the effective curvature radii ρ_{eff} as a function of triangulation size N , for all three ensembles, where the largest δ included in the ρ_{eff} fits, δ_{max} , is scaled according to eq. (5.4), with $N_{ref} = 80k$. The results presented are obtained from fits to curvature profiles of $(D = 4)$ -sphere curvature profiles. Linear fits are made, shown in orange. The resulting power law exponents are presented in the legends.

Table 5.5: Values of \mathcal{D} found for a range of sphere dimensions D , obtained using the scaling δ_{max} according to eq. (5.4). Here, N_{ref} is set to $80k$. The discretization radii δ_{discr} are set to the values found in section 5.4.2. Column labels \mathcal{T}_C , \mathcal{T}_{RD} , and \mathcal{T}_{MD} denote the triangulation ensemble used for obtaining the results presented.

D	\mathcal{D}		
	\mathcal{T}_C	\mathcal{T}_{RD}	\mathcal{T}_{MD}
2	4.19 ± 0.09	4.27 ± 0.08	4.31 ± 0.08
3	4.03 ± 0.09	4.09 ± 0.08	4.12 ± 0.08
4	4.00 ± 0.09	4.06 ± 0.08	4.09 ± 0.08
5	3.99 ± 0.09	4.04 ± 0.09	4.05 ± 0.08

5.5 Summary of incremental improvements

The present chapter presents incremental improvements on the methods presented in [7]. Additionally, argumentation is presented to justify these improvements. While those pieces of justification are necessary for completeness, they may have obscured the key takeaways. Therefore, the most important improvements and results are reiterated here.

In section 5.2, measurements that replicate the methods of [7] have been presented, that is, average sphere distance measurements in the combinatorial ensemble. While the present results confirm the

overall conclusion of [7], statistically significant differences in the results were noted. Section 5.3 contains the results for average sphere distance measurements in the degenerate ensembles. Again, the conclusion from these results is the same: The volume scaling exponent \mathcal{D} and the sphere dimension D agree best at $D = 5$. However, the poor fits of Figures 5.1 and 5.3 suggest the presence of discretization and finite-size effects.

In [7], possible discretization effects are dealt with by excluding the data points of the curvature profiles with $\delta < \delta_{discr} = 5$. In section 5.4.2 it has been shown that for the combinatorial ensemble, discretization effects are still present at $\delta_{discr} = 5$, and that setting $\delta_{discr} = 7$ is a better choice for excluding discretization effects. Similarly, $\delta_{discr} = 6$ is a better choice for the degenerate ensembles. With the new value $\delta_{discr} = 7$ for the combinatorial ensemble, these results now also visibly show finite-size effects, as can be seen in Fig. 5.6. Their absence until now had been conspicuous, since finite-size effects were present in the measurements for the degenerate ensembles.

The presence of finite-size effects has been addressed in section 5.4.3. To this end, two methods have been presented. The first is more radical in discarding data points: All data points at a triangulation size where finite-size effects are seen are discarded. The second method relies on more refined assumptions regarding the presence of finite-size effects: The distance δ at which finite-size effects occur is assumed to be proportional to the distance where finite-size effects occur in the measurements for the Hausdorff dimension. Only data points that are suspected of finite-size effects using this assumption are discarded. Both methods lead to the same conclusion: The volume scaling exponent \mathcal{D} and the sphere dimension D agree best at $D = 4$, for all three ensembles. Notable is the case of the second method, where this agreement is (nearly) within one error bar (see Table 5.5), showing not only good resemblance to the four-sphere, but also that the result is independent of discretization.

Lastly, let us illustrate the improvement in fit quality we obtain by reproducing the curve collapse of Figure 6 of [7] for the combinatorial ensemble, before and after the aforementioned improvements to the methodology. The 2D EDT average sphere distance curves are rescaled by their effective curvature radius ρ_{eff} , obtained before and after improvements. Both are shown in Figure 5.9 with the $D = 4$ continuum sphere curve with a best fit vertical shift. After the improvements, the collapse of the 2D EDT average sphere distance curves is better both to each other, and to the continuum sphere curve, for the data points considered.

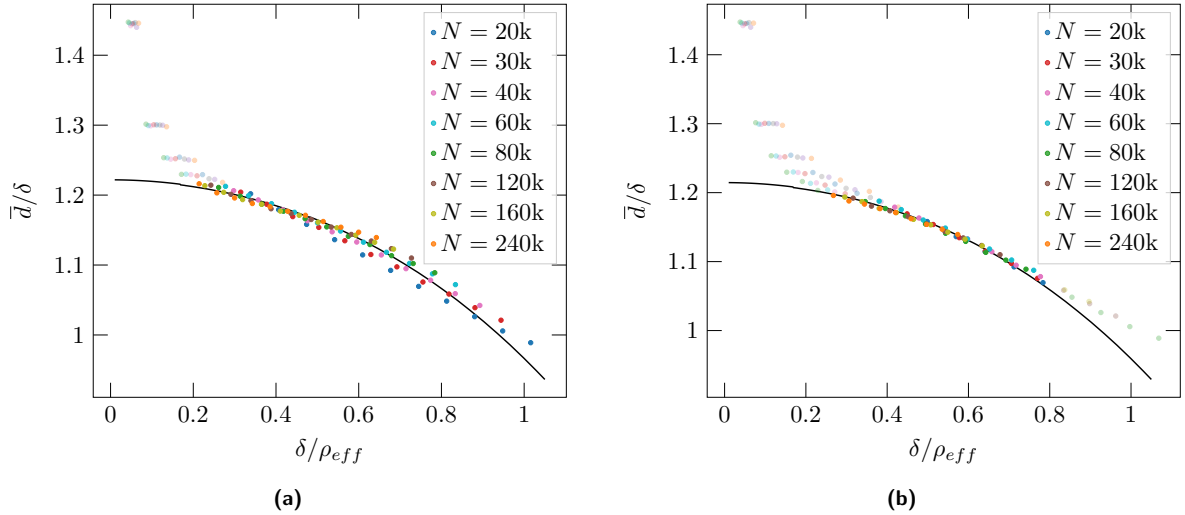


Figure 5.9: Curve collapse of the 2D EDT average sphere distance measurements, rescaled by their effective curvature radius ρ_{eff} for volumes in the range $N \in [20k, 240k]$, and sphere dimension $D = 4$. Results obtained with $\delta_{discr} = 5$ and constant $\delta_{max} = 16$ are shown in (a), results obtained with $\delta_{discr} = 7$ and scaling δ_{max} according to eq. (5.4) are shown in (b). Both are presented with the 4-sphere average sphere distance curve, vertically shifted to best fit the data. Data points with $\delta < \delta_{discr}$ or $\delta > \delta_{max}$ are not used in the fitting procedure, and are shown with faint coloring.

Chapter 6

Conclusion

Previous work concluded that the curvature properties of 2D Euclidean Dynamical Triangulations (2D EDT) resemble those of a ($D = 5$) sphere [7], by performing average sphere distance measurements on combinatorial triangulations. While there is no prediction for which D -sphere's curvature properties resemble those of 2D EDT, the result $D = 5$ was unexpected, as it did not equal any of the known fractal dimensions characterizing 2D EDT, which are either 2 or 4. The aim of the present work was to investigate this issue in more detail by measuring the average sphere distance in two additional ensembles of triangulations, the restricted degenerate and maximally degenerate ensembles.

As validation of the simulations, the Hausdorff dimension d_H was measured. The results are close to, but not within error bars of the known value $d_H = 4$. The closest result that was extracted using curve collapse was $d_H = 3.91 \pm 0.01$, which was found for the maximally degenerate ensemble of triangulations. The deviation from the known value is suspected to be caused by finite-size effects. Going to larger triangulation sizes will likely bring the estimate closer to the known value.

Measurements of the average sphere distance on combinatorial triangulations with a methodology similar to that of [7] found a compatible result. The results for the degenerate ensembles also led to the same conclusion. However, further analysis in which data points subject to discretization effects and finite size effects were removed according to additional, well-motivated prescriptions showed that the curvature properties of 2D EDT are best approximated by those of the four-sphere. Good agreement with $D = 4$ is found in all three ensembles considered.

Appendix A

Link and vertex picture equivalence

In section 2.2.1, three formulations for the definition of a combinatorial manifold are given. The equivalence between two formulations, using either the *link picture* or the *vertex picture*, is not shown in the main text. In this appendix, a proof for the equivalence is presented. Let us restate the definitions for the combinatorial ensemble using the two aforementioned pictures:

1. In the *link picture*: the link lk of every edge and vertex in the triangulation is homeomorphic to S^0 and S^1 respectively.
2. In the *vertex picture*: The vertices of any edge and triangle are distinct from each other, and each edge and triangle is uniquely described by the list of its vertices.

In the following discussion, these definitions may be referred to as rulesets 1 and 2 respectively.

The key idea is to construct a generic neighborhood of radius 1 around a vertex v . First, a triangle is considered, with v at one of its corners. All edge-to-edge and planar gluings using these elements are tested against both rulesets. Then, a second triangle is added, glued to the first triangle, such that vertex v is also a vertex of this new triangle. Again, all gluings using these elements are tested against both rulesets. This process is continued until either the rulesets disagree on the legality of a gluing, or the agreement of the rulesets can be extrapolated indefinitely after a certain point in the process. In the latter case, the rulesets place the exact same demands on the neighborhood of any vertex in the triangulation, and are therefore equivalent.

As mentioned, start with a triangle that has a vertex v at one of its corners. The other vertices are labelled x_1 and x_2 . This setup is shown in Fig. A.1. Three gluings are possible: $e(x_1, x_2)$ to either $e(v, x_1)$ or $e(v, x_2)$, and $e(v, x_1)$ to $e(v, x_2)$, where the notation $e(x, y)$ denotes the edge with endpoints x and y . The first two of these gluings are related by symmetry, and testing either one to ruleset 1 we find that $lk(v) \not\cong S^1$. The other gluing, $e(v, x_1)$ to $e(v, x_2)$, results in the following edge links: $lk(e(v, x_1)) = lk(e(v, x_2)) = \emptyset \not\cong S^0$. It follows that ruleset 1 does not allow for a single triangle neighborhood of a vertex. Ruleset 2 also forbids all gluings. Any gluing will inevitably identify one of the vertices with another, causing there to be repeated vertices in the list of vertices that describe the triangle.

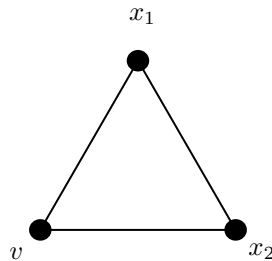


Figure A.1: Vertex v , at the corner of a single triangle

Now all gluings concerning a single triangle have been tested against the rulesets, let us consider a neighborhood consisting of two triangles, shown in Fig. A.2. A second triangle is present, as well as a fourth vertex, labelled x_3 . The gluings that identify an edge with another edge of the same triangle are excluded, since these are already covered in the single triangle case. That leaves the following three

gluings: $e(v, x_1)$ to $e(x_2, x_3)$, $e(v, x_3)$ to $e(x_1, x_2)$, and $e(v, x_1)$ to $e(v, x_3)$. Again, the first two gluings are related by symmetry, and both gluings give $lk(v) \cong S^1$. The latter gluing, $e(v, x_1)$ to $e(v, x_3)$, is excluded by ruleset 1, since after this gluing we have $lk(e(v, x_2)) = x_1 = x_3 \cong S^0$. The three aforementioned gluings are also excluded by ruleset 2, since after each of these gluings the two triangles share the same list of vertices. Consequently, the lists of vertices no longer describe the triangles uniquely.

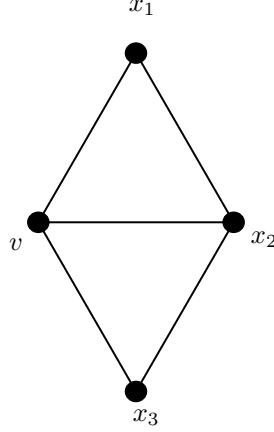


Figure A.2: Vertex v , at the corner of two triangles.

Consider now a neighborhood of three triangles, shown in Fig. A.3. Again, the addition of a triangle requires a new vertex, labelled x_4 . There are four possible gluings that are not already covered by the one- or two-triangle case: $e(x_1, x_2)$ to $e(x_3, x_4)$, $e(v, x_1)$ to $e(x_3, x_4)$, $e(v, x_4)$ to $e(x_1, x_2)$, and $e(v, x_1)$ to $e(v, x_4)$. The first gluing, and the second and third gluing, which are related by symmetry, give $lk(v) \cong S^1$.

The last gluing, $e(v, x_1)$ to $e(v, x_4)$, does give $lk(v) \cong S^1$. Furthermore, for every $x_i = x_1, x_2, x_3$ it also holds that $lk(e(v, x_i)) = x_j, x_k \cong S^0$, where $i \neq j \neq k$. This gluing results in a neighborhood of v that is allowed by ruleset 1. Next, the three-triangle gluings are tested against ruleset 2: The arguments that forbid identifying v to x_i have been covered in the one triangle case. Furthermore, no two vertices x_i and x_j can be identified with each other, without gluing $e(v, x_i)$ to $e(v, x_j)$. Otherwise, the two edges would be distinct, but would have equal vertex lists: $\{v, x_i = x_j\}$. That leaves one option: gluing $e(v, x_1)$ to $e(v, x_4)$.

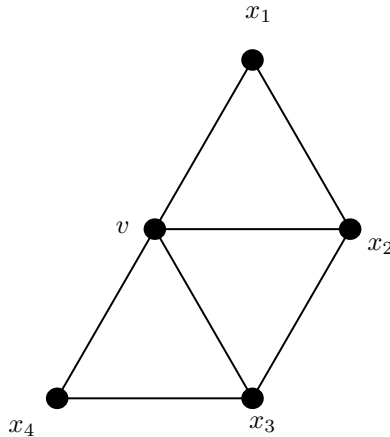


Figure A.3: Vertex v , at the corner of three triangles.

Finally, consider a neighborhood of $q > 3$ triangles, as shown in Fig. A.4. The arguments of the three triangle case apply to the $q > 3$ case as well. Both rulesets rule out any gluing, except $e(v, x_1)$ to $e(v, x_{q+1})$.

Both rulesets 1 and 2 place the same restrictions on a triangulation. It follows that the *link picture* and *vertex picture* definitions of the combinatorial ensemble are equivalent.

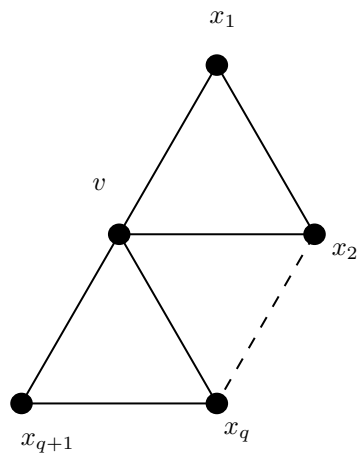


Figure A.4: Vertex v , at the corner of q triangles.

Appendix B

Vertex links in the degenerate ensembles

In Figures 2.5 and 2.7, examples of vertex links are presented for the restricted and maximally degenerate ensemble, respectively. In this appendix, we present what general vertex link looks like in the two degenerate ensembles. Let us start with the restricted degenerate ensemble.

B.1 Restricted degenerate ensemble

The key idea is to construct a general neighborhood of v , only keeping in mind the details that are relevant for $lk(v)$. The general neighborhood of v in the restricted degenerate ensemble is constructed by starting with the general neighborhood of v in the combinatorial ensemble, as defined in section 2.2.1, and then exploring which additional gluings are available for the neighborhood of v in the restricted degenerate ensemble \mathcal{T}_{RD} . This exploration is performed by iteratively considering the simplest possible additions to the neighborhood, until all possibilities can be taken into account recursively.

Consider an edge e_0 connecting v to a vertex $w \in lk(v)$, shown in Figure B.1. In the restricted degenerate ensemble, there could be more than one distinct link connecting v to w . Let us start with the simplest case where instead of the single edge of before, two distinct edges e_1 and e_2 connect v to w , shown in Figure B.2. This substitution, that brings the case of Figure B.1 to the case of Figure B.2 is labelled (i). The shaded area denotes the fact that between these edges there could be any piece of restricted degenerate triangulation with disk topology, and with a boundary of length $l = 2$. Here, the first recursive argument is made: substitution (i) can be performed at edge e_1 or e_2 . This way, the case of three edges connecting v to w is made. Repeated application of substitution (i) causes an arbitrary number of edges to connect v to w . It follows that although an arbitrary number of edges is allowed to connect v to w , the general neighborhood of v is determined by exploring the case of only two edges connecting v to w .

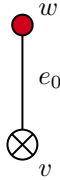


Figure B.1: Vertex v , with edge e_0 connecting it to vertex w , part of $lk(v)$, depicted in red.

Let us now consider the smallest piece of triangulation that could make up the shaded area of Figure B.2. For the \mathcal{T}_{RD} , this consists of two triangles that share two of their edges, shown in Figure B.3. Larger disk triangulations with boundary length 2 are obtained by one of the following four substitutions:

- (ii) replacing e_4 by a two-loop,
- (iii) replacing e_3 by a two-loop,
- (iv) replacing both e_3 and e_4 by a two-loop, or

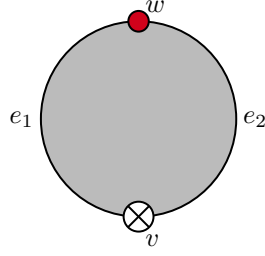


Figure B.2: Vertex v , with edges e_1 and e_2 connecting it to vertex w , part of $lk(v)$, depicted in red. The shaded area represents any piece of restricted degenerate triangulation with disk topology and boundary length $l = 2$.

(v) replacing e_3 and e_4 together by a four-loop.

The results of these substitutions are shown in Figure B.4. The result of substitution (ii), shown in Figure B.4a, is explored using the following recursive arguments: the two-loop of edges e_4 and e_5 , is of the exact same nature as the two-loop of Figure B.2. Substitutions made there can be made here as well. Furthermore, the edges e_4 and e_5 can be subject to substitution (i). Lastly, any pairing of one of the edges e_4 and e_5 with e_3 is of the same shape as the edges e_3 and e_4 of Figure B.3, and the substitutions (iii) to (v) can be made.

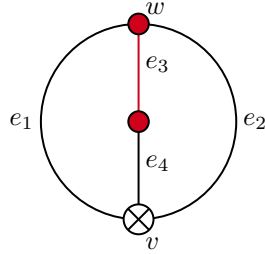


Figure B.3: The smallest restricted degenerate disk triangulation with boundary length $l = 2$, enclosed by edges e_1 and e_2 . The vertex v is marked with a cross, parts of $lk(v)$ are shown in red.

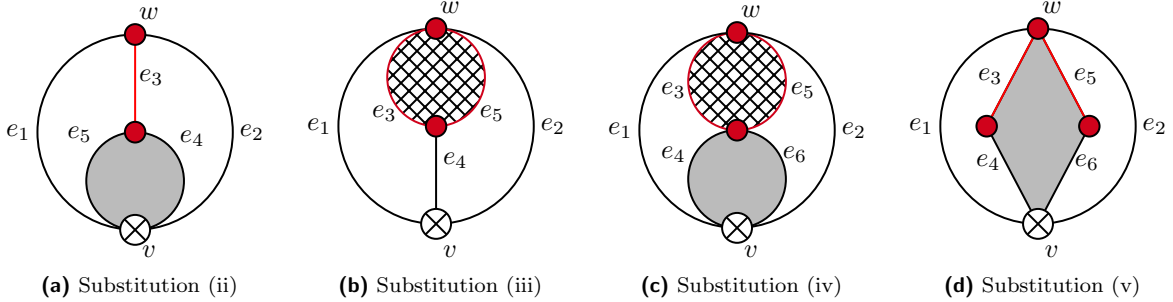


Figure B.4: The results of substitutions (iii) to (v). The vertex v is marked with a cross, parts of $lk(v)$ are shown in red. The shaded regions denote arbitrary restricted degenerate disk triangulations with suitable boundary length, the crosshatching denotes pieces of triangulation that are irrelevant for $lk(v)$.

The result of substitution (iii), shown in Figure B.4b is explored. The piece of triangulation that sits inside the two-loop is irrelevant for the link of v . Furthermore, edge e_4 can be subject to substitution (i). Lastly, any pairing of one of the edges e_3 and e_5 with e_4 is of the same shape as the edges e_3 and e_4 of Figure B.3, and the substitutions (iii) to (v) can be made.

The result of substitution (iv), shown in Figure B.4c, is also explored by recognizing previous steps. The two-loop of edges e_4 and e_6 is of the same nature as the two-loop of Figure B.2. The piece of triangulation that sits inside the two-loop of edges e_3 and e_5 is irrelevant for the link of v . Lastly, any pairing of one of the edges e_4 and e_6 with either e_3 or e_5 is of the same shape as the edges e_3 and e_4 of Figure B.3, and the substitutions (iii) to (v) can be made.

The result of substitution (v) requires some further investigation before it can be explored fully by recognizing previous steps. The edges e_3 , e_4 , e_5 and e_6 form a four-loop, and consequently any piece

of restricted degenerate triangulation with disk topology with boundary length $l = 4$ can be placed in between, indicated by the shaded area in Figure B.4d. The smallest piece restricted degenerate disk triangulation with boundary length $l = 4$ is two triangles meeting along one edge. This piece can be placed in the aforementioned four-loop in two inequivalent ways, both shown in Figure B.5. The substitutions of Fig. B.5a and Fig. B.5b are labelled (v)a, (v)b, respectively. The result of substitution (v)a is fully explored by recognizing the following: edges e_4 , e_6 and e_7 can be subject to substitution (i). Furthermore, any pair of either e_4 , e_6 or e_7 , with either e_3 or e_5 , can be subject to substitutions (iii) to (v). The result of substitution (v)b is also fully explored by recognizing previous steps. First, note that the piece of triangulation that sits inside the three-loop formed by edges e_3 , e_5 and e_7 is not relevant for $lk(v)$. Furthermore, edges e_4 and e_6 are subject to substitution (i). Any pair of either e_4 or e_6 , with either e_3 , e_5 or e_7 , can be subject to substitutions (iii) to (v).

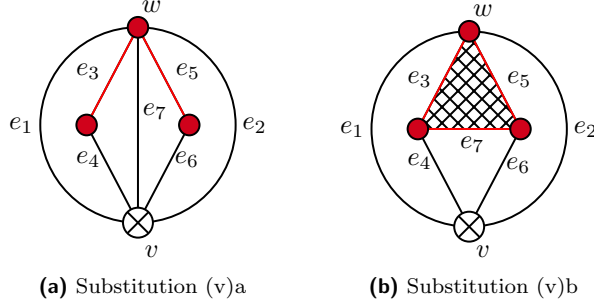


Figure B.5: The two inequivalent ways to place two triangles in the four-loop of Fig. B.4d. These are the results of substitutions (v)a and (v)b. The vertex v is marked with a cross, parts of $lk(v)$ are shown in red. The crosshatching denotes pieces of triangulation that are irrelevant for $lk(v)$.

Note how substitutions (iii) and (iv) create a two-loop in $lk(v)$. If applied to a pair of edges where one of the edges is part of a loop in the link, the substitution (v)b increases the length of this loop by one. If it is not applied to edges that are part of a loop in the link, it creates a three-loop in the link. Together with the effects that the other substitutions have on the link, we come to the following conclusion about the general link in the restricted degenerate ensemble: the link of any vertex of a restricted degenerate triangulation is a tree of edges, and of n -loops, with $n \geq 2$, where the intersection of two of these loops can at most be a single vertex. An example of a link that is possible in the restricted degenerate ensemble is shown in Figure B.6.

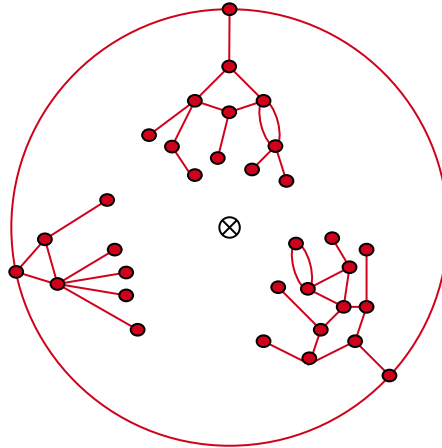


Figure B.6: The general link (in red) of a vertex (marked with cross), in the restricted degenerate ensemble. For clarity, some vertices of the link, and edges that are not part of the link are not shown.

B.2 Maximally degenerate ensemble

Constructing the general vertex link in the maximally degenerate ensemble follows the construction of the restricted degenerate ensemble, with the following alteration: the maximally degenerate ensemble

allows for a second disk triangulation with boundary length $l = 2$ that can be placed in the two-loop after substitution (i) in two inequivalent ways, shown in Figure B.7. Either a one-loop is placed at v , or at w . In both cases, the edges e_1 and e_2 can both be subject to substitution (i). The piece of triangulation within the one-loop formed by edge e_3 in Figure B.7b is not relevant for the link of v , indicated with crosshatching.

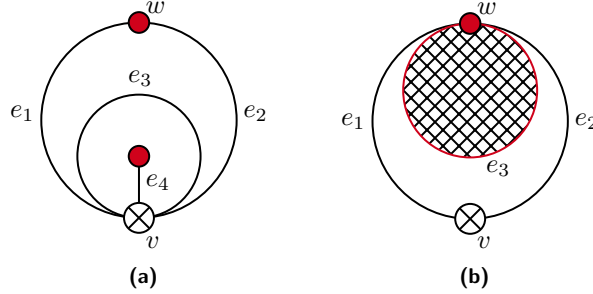


Figure B.7: The two inequivalent ways in which the $l = 2$ disk triangulation that is now allowed in the maximally degenerate ensemble can be placed in the two-loop after substitution (i). The vertex v is marked with a cross, parts of $lk(v)$ are shown in red. The crosshatching denotes pieces of triangulation that are irrelevant for $lk(v)$.

The one-loop e_3 , starting and ending in v , of Figure B.7a, is a case that has not been seen before. Similar to substitution (i), this edge can be replaced by a two-loop, and similar further substitutions follow. However, the consequences for the link are different, since before one of the vertices of the edge subject to the substitution was part of the link. Recall that the first step after replacing the edge of interest with a two-loop, was to put the smallest disk triangulation with boundary length $l = 2$ inside the two loop. The maximally degenerate ensemble allows for two different two-triangle disk triangulations with boundary length $l = 2$. Placing these in the two-loop that is substituted for edge e of Figure B.7a gives the results presented in Figure B.8. Here, the vertex v is drawn in two places for clarity.

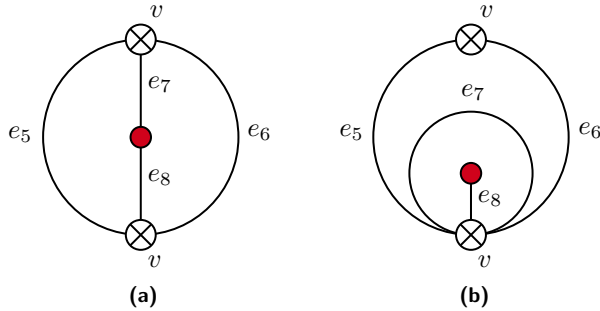


Figure B.8: The two possible two-triangle substitutions possible for the edge e_3 of Fig. B.7a. The vertex v is marked with a cross and is drawn in two places for clarity, parts of $lk(v)$ are shown in red.

All elements of the situation presented in Fig. B.8b have been explored before. The pair of edges e_7 and e_8 of Fig. B.8a, with a vertex belonging to the link in the middle, has not been explored before. Again, the substitutions that are possible here are similar to the substitutions (iii) to (v) available for edges e_3 and e_4 of Fig. B.3, but the consequences for the link are different. The four possible substitutions are laid out in Figure B.9. Again, the vertex v is drawn in two places for clarity. Note that the substitution of Fig. B.9a corresponds to substitutions (ii) and (iii), Fig. B.4c corresponds to (iv), Fig. B.9c corresponds to (v)a, and Fig. B.9d corresponds to substitution (v)b. All elements of the situations presented in Fig. B.9 have been explored before, and consequently the exploration of the maximally degenerate vertex link is complete.

Note how in the maximally degenerate ensemble a link vertex or edge can be present that is disconnected from the rest of the link. Furthermore, one-loops in the link are allowed. It follows that the link of a vertex in the maximally degenerate ensemble consists of trees of edges and n -loops with $n \geq 1$, which are not necessarily connected. An example is shown in Fig. B.10. An example of a link that is possible in the maximally degenerate ensemble is shown in Figure B.10.

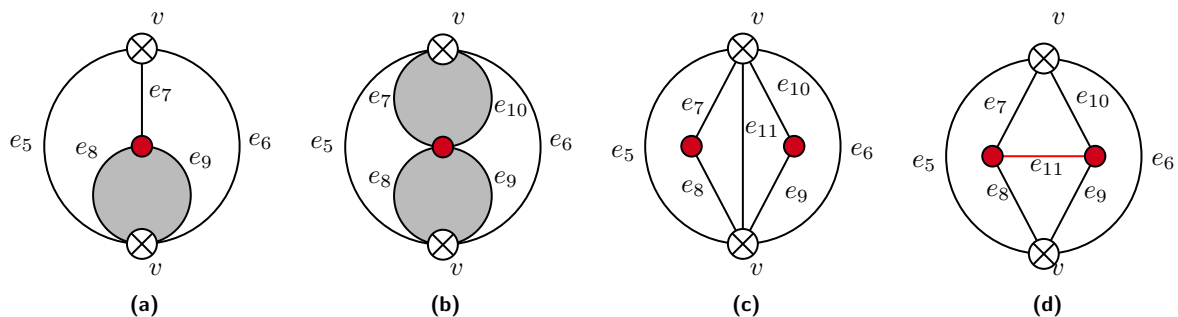


Figure B.9: The four substitutions possible for the pair of edges e_7 and e_8 of Fig. B.8a. The vertex v is marked with a cross and is drawn in two places for clarity, parts of $lk(v)$ are shown in red. The shaded regions denote arbitrary restricted degenerate disk triangulations with suitable boundary length.

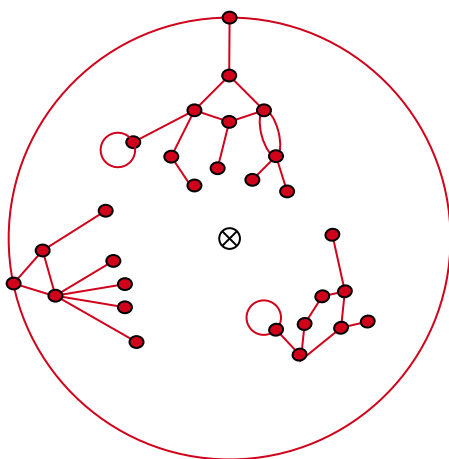


Figure B.10: The general link (in red) of a vertex (marked with cross), in the maximally degenerate ensemble. For clarity, some vertices of the link, and edges that are not part of the link are not shown.

Appendix C

Average sphere distance on a hypersphere

In this appendix, we will derive the exact integral expression for the average sphere distance on a continuum sphere of dimension $D \geq 2$, which is referred to in section 2.4.1. Consider first the case of the 2-sphere. This case allows for an easy embedding in \mathbb{R}^3 , and is therefore an intuitive example. To evaluate an average sphere distance, the setup of Fig. 2.8 must be implemented. Note that ϵ is not set equal to δ here, unlike the applications presented in the present work. Due to the symmetry of the sphere the average sphere distance does not depend on the exact location of p and p' , on the distance δ that separates them. Consequently, a manifold average over δ -separated center points p, p' is unnecessary. A convenient choice for p, p' can therefore be made without loss of generality, provided $d(p, p') = \delta$. Using a spherical coordinate system in \mathbb{R}^3 , the 2-sphere is the surface of constant radius ρ . Every point is described by a polar angle $\theta \in [0, \pi]$, and an azimuth angle $\phi \in [0, 2\pi)$.

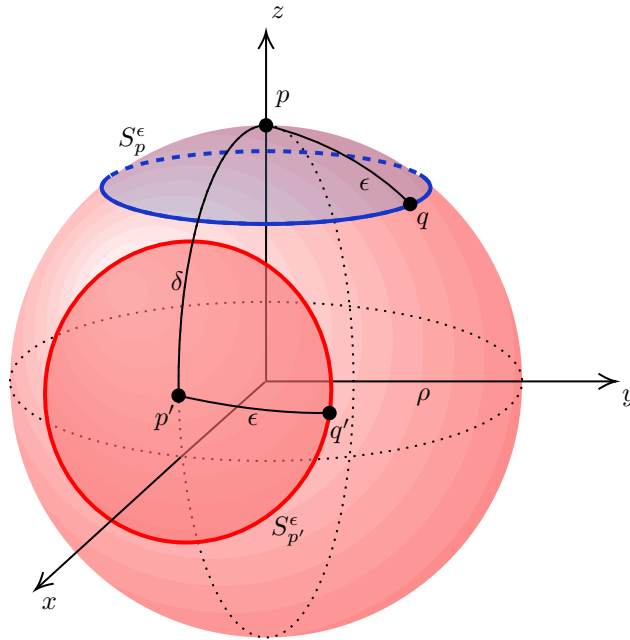


Figure C.1: Application to the 2-sphere of radius ρ of the general average sphere distance construction presented in Fig. 2.8. The sphere S_p^ϵ , with radius ϵ and center point p at the north pole, is shown in blue. An arbitrary point q on this sphere is marked. The sphere $S_{p'}^\epsilon$, with center point p' at the $\phi = 0$ meridian, is shown in red. An arbitrary point q' on this sphere is marked. Note that these spheres are 1-spheres, i.e., the bold and colored circles pictured. The shaded areas they enclose are for clarity only. Cartesian axes x, y , and z are shown in black. To avoid clutter, no spherical coordinate system is pictured. The usual set up is implied however, with θ the polar angle to the Cartesian z -axis, and ϕ the azimuth angle, clockwise around the z -axis. The angles are defined such that the point $\theta = \pi/2, \phi = 0$ sits at the x -axis.

The construction that will be used is shown in Fig. C.1. The point p is placed at the north pole,

$\theta = 0$. The point p' is placed at the $\phi = 0$ meridian, a geodesic distance δ from p . Since geodesics on the sphere are arcs of great circles, the polar angle of p' is $\theta = \delta/\rho$. Similarly, the points on S_p^ϵ all sit at $\theta = \epsilon/\rho$. These points are all described by only one angle $\alpha \in [0, 2\pi)$, here $\alpha = \phi$. In Cartesian coordinates, the vector from the origin to point $q(\alpha)$ is given by¹:

$$\vec{q}(\alpha) = \begin{pmatrix} z \\ x \\ y \end{pmatrix} = \rho \begin{pmatrix} \cos(\epsilon/\rho) \\ \sin(\epsilon/\rho) \cos(\alpha) \\ \sin(\epsilon/\rho) \sin(\alpha) \end{pmatrix}. \quad (\text{C.1})$$

Similarly, let $\beta \in [0, 2\pi)$ describe the points on $S_{p'}^\epsilon$. Using a rotation, the vector pointing to the points on $S_{p'}^\epsilon$ is

$$\vec{q}'(\beta) = M(\delta/\rho) \cdot \vec{q}(\beta) = \begin{pmatrix} \cos(\delta/\rho) & -\sin(\delta/\rho) & 0 \\ \sin(\delta/\rho) & \cos(\delta/\rho) & 0 \\ 0 & 0 & 1 \end{pmatrix} \cdot \begin{pmatrix} \cos(\epsilon/\rho) \\ \sin(\epsilon/\rho) \cos(\beta) \\ \sin(\epsilon/\rho) \sin(\beta) \end{pmatrix}. \quad (\text{C.2})$$

The angle between $\vec{q}(\alpha)$ and $\vec{q}'(\beta)$ is found from their inner product. Again invoking the fact that geodesics are great circles, the distance between a point on S_p^ϵ parametrized by α , and a point on $S_{p'}^\epsilon$ parametrized by β is given by

$$d(\alpha, \beta) = \rho \arccos \left(\frac{\vec{q}(\alpha) \cdot \vec{q}'(\beta)}{\|\vec{q}(\alpha)\| \|\vec{q}'(\beta)\|} \right) = \rho \arccos \left(\frac{\vec{q}(\alpha) \cdot M(\delta/\rho) \cdot \vec{q}(\beta)}{\rho^2} \right). \quad (\text{C.3})$$

Finally, using equation (2.19), one finds

$$\frac{\bar{d}}{\delta} = \frac{\rho}{\delta} \frac{1}{(2\pi)^2} \int_0^{2\pi} d\alpha \int_0^{2\pi} d\beta \arccos \left(\frac{\vec{q}(\alpha) \cdot M(\delta/\rho) \cdot \vec{q}(\beta)}{\rho^2} \right). \quad (\text{C.4})$$

Inspecting equations (C.1), (C.2), and (C.4), \bar{d}/δ is only a function of δ/ρ and ϵ/ρ . In fact, this turns out to be true for $D > 2$ as well. Therefore, one can consider only the unit sphere without loss of generality. In that case ϵ/ρ and δ/ρ become ϵ and δ . For this reason, the rest of this section will only consider the unit sphere. To recover a non-unit sphere, only the substitutions $\epsilon \rightarrow \epsilon/\rho$ and $\delta \rightarrow \delta/\rho$ need to be made.

It is straightforward to generalize the previous calculation to $D > 2$. The spherical coordinates are now $\rho, \phi_1, \dots, \phi_D$. Here, $\phi_D \in [0, 2\pi)$, and $\phi_1, \dots, \phi_{D-1} \in [0, \pi]$. Points on S_p^ϵ are described by $D-1$ angles, denoted by $\{\alpha_i\} = \{\alpha_1, \dots, \alpha_{D-1}\}$. In Cartesian coordinates, these points are given by

$$\vec{q}(\{\alpha_i\}) = \begin{pmatrix} \cos(\epsilon) \\ \sin(\epsilon) \cos(\alpha_{D-1}) \\ \vdots \\ \sin(\epsilon) \sin(\alpha_{D-1}) \cdots \cos(\alpha_1) \\ \sin(\epsilon) \sin(\alpha_{D-1}) \cdots \sin(\alpha_1) \end{pmatrix}. \quad (\text{C.5})$$

Similarly, the points on $S_{p'}^\epsilon$ are parametrized by the angles $\{\beta_i\} = \{\beta_1, \dots, \beta_{D-1}\}$, and are again found by applying a rotation to $\vec{q}(\{\beta_i\})$:

$$\vec{q}'(\{\beta_i\}) = M(\delta) \cdot \vec{q}(\{\beta_i\}) = \begin{pmatrix} \cos(\delta) & -\sin(\delta) & & \\ \sin(\delta) & \cos(\delta) & & \\ & & O_{2,D-1} & \\ & & & I_{D-1} \end{pmatrix} \cdot \vec{q}(\{\beta_i\}), \quad (\text{C.6})$$

where $O_{m,n}$ denotes the $m \times n$ null matrix, and I_n the $n \times n$ identity matrix. Using the same arguments as for the $D = 2$ case, one finds the following for the geodesic distance between $q(\{\alpha_i\})$ and $q'(\{\beta_i\})$:

$$d(\{\alpha_i\}, \{\beta_i\}) = \arccos(\vec{q}(\{\alpha_i\}) \cdot M(\delta) \cdot \vec{q}(\{\beta_i\})). \quad (\text{C.7})$$

Finally, averaging is performed over the volumes of S_p^ϵ and $S_{p'}^\epsilon$, with volume elements

$$d\Omega_{\{\alpha_i\}} = \sin^{D-2}(\alpha_1) \cdots \sin(\alpha_{D-2}) \prod_{i=1}^{D-1} d\alpha_i, \quad (\text{C.8})$$

¹Note the unusual order of the Cartesian coordinates in the vector. When generalizing to $D > 2$, this ordering is more convenient to notate.

and $d\Omega_{\{\beta_i\}}$ likewise. Then, \bar{d} is given by

$$\bar{d} = \frac{1}{(V_{D-1}(1))^2} \int d\Omega_{\{\alpha_i\}} \int d\Omega_{\{\beta_i\}} d(\{\alpha_i\}, \{\beta_i\}), \quad (\text{C.9})$$

where $V_n(\rho)$ denotes the volume of an n -sphere of radius ρ .

Let us end this appendix with some remarks regarding the numerical integration of the integral in eq. C.9. Note how the dimension of the domain of integration is $2(D-1)$. As a consequence, numerical integration for higher values of D quickly becomes computationally expensive. For this reason, we have determined the $D=5$ curve in Fig. 2.9 by using Monte Carlo integration. Furthermore, the computation time can be roughly halved by using the symmetry of the system: either α_{D-1} or β_{D-1} can be integrated from 0 to π , instead of 2π . Afterwards the result must of course be multiplied by 2 to compensate, but halving the domain of integration saves much more time than a single multiplication would ever cost. While this speedup is helpful, for higher dimensions D it cannot counteract the inherent exponential growth in computation time.

Appendix D

Edge flip ergodicity

In this appendix we show that the edge flip is an ergodic update for spherical 2D degenerate triangulations of fixed size. This property is used in section 2.5. To show that the edge flip is an ergodic update, an approach similar to that of [20] is used. It is known that the move is ergodic for combinatorial triangulations. Since $\mathcal{T}_{MD} \supset \mathcal{T}_{RD} \supset \mathcal{T}_C$, it is sufficient to show that for any triangulation in \mathcal{T}_{MD} there exists a finite number of moves that reaches a triangulation in \mathcal{T}_{RD} , and likewise that there exists a finite number of moves for any triangulation in \mathcal{T}_{RD} to a triangulation in \mathcal{T}_C .

D.1 Removing one-necks

To show the former, consider the case of an edge with overlapping endpoints: a one-neck, or tadpole in the dual graph (the equivalence of which has been shown in section 2.2.1). The general case is shown in Fig. D.1a. The dual graph is considered, and unless mentioned otherwise, the terms vertex, edge, and face refer to the elements of the dual graph. Edge e has face v at both sides, i.e., in the non-dual graph both endpoints are vertex v . The dashed area denotes any planar ϕ^3 diagram with one leg, with its size constrained by the size of the triangulation it is part of. When edge e is followed into the dashed area, one is guaranteed to hit a vertex. This vertex is either connected to two tadpoles, or one self-energy. These options are presented in Figures D.1b and c respectively. The result of flipping edge e in both cases is shown in Fig. D.2. In both cases, the edge e is no longer a one-neck after the flip. Furthermore, any one-necks that are left after the flip were there beforehand. These can be given the same treatment as the original one-neck. This way, the dashed area can be recursively explored, removing all one-necks one encounters in the process until a self-energy is made at the end of every branch. This is guaranteed to happen in a finite number of steps due to the finiteness of the original tadpole diagram.

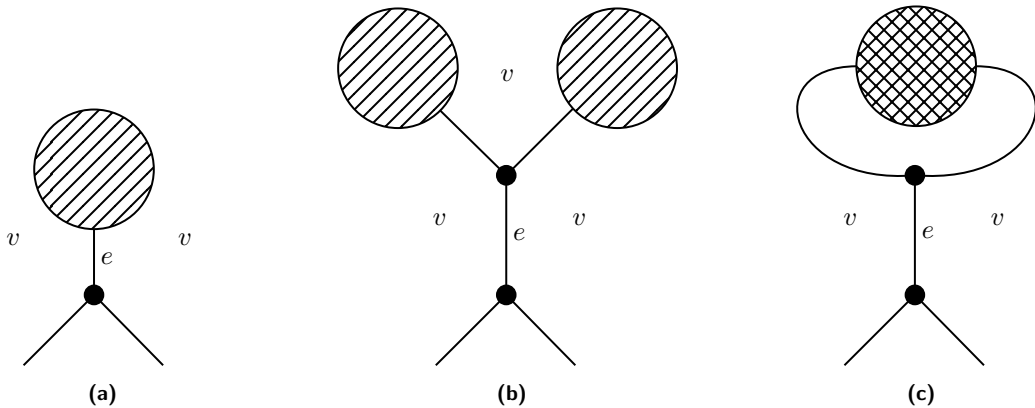


Figure D.1: The general case of an edge e with coinciding endpoints in v , represented as a dual graph, in (a). The dashed area denotes any planar ϕ^3 diagram with one leg. Following the dual edge e into this area, a dual vertex is encountered. This vertex is either connected to two tadpole diagrams, shown in (b), or to a self-energy diagram, shown in (c). Here, the crosshatched area denotes any planar ϕ^3 diagram with two legs.

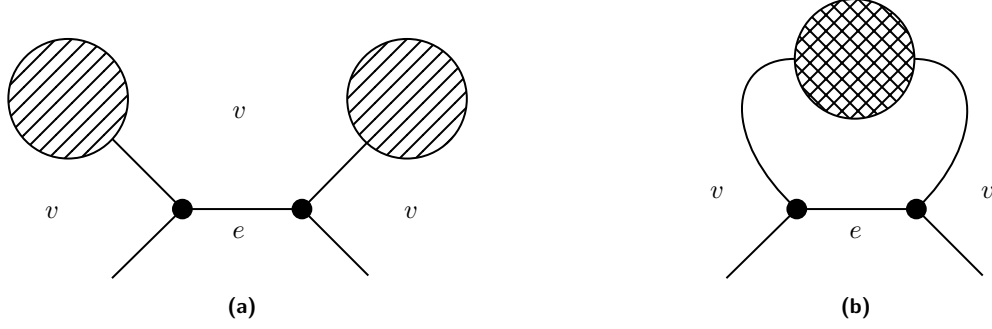


Figure D.2: Results of flipping edge e in Figures D.1b and D.1c respectively.

D.2 Removing two-necks

To show it is possible to reach a triangulation in \mathcal{T}_C from any triangulation in \mathcal{T}_{RD} , consider the general case of a two-neck, that is, two edges that share their endpoints. The dual graph of such a gluing is presented in Fig. D.3a. The crosshatched area denotes any planar ϕ^3 diagram with two legs. The simplest case of this, where this crosshatched area is just a single edge, is shown in Fig. D.3b. Here, there is no two-neck since, e_1 is the same edge as e_2 . Therefore, this case can be ignored in the following arguments. That case aside, Fig. D.3a shows the general two-neck: edges e_1 and e_2 both connect v_1 to v_2 . Similar to the treatment of the one-neck, consider the options one could encounter when traversing from e_1 to e_2 along the dual graph. Since tadpoles can be excluded, the only possibility is that of Fig. D.3c. The result of flipping the edge e_1 is shown in Fig. D.4. Due to the symmetry, only the flip of e_1 is considered without loss of generality. Note that after the flip, edge e_1 does not connect v_1 to v_2 anymore, and thus the two-neck is removed. Furthermore, no new self-energies or tadpoles are made by performing the flip. Again, due to the finiteness of the original crosshatched diagram, this process only has to be repeated a finite number of times until all obtained crosshatched diagrams are simply single, that is, the diagram in Figure D.3b.

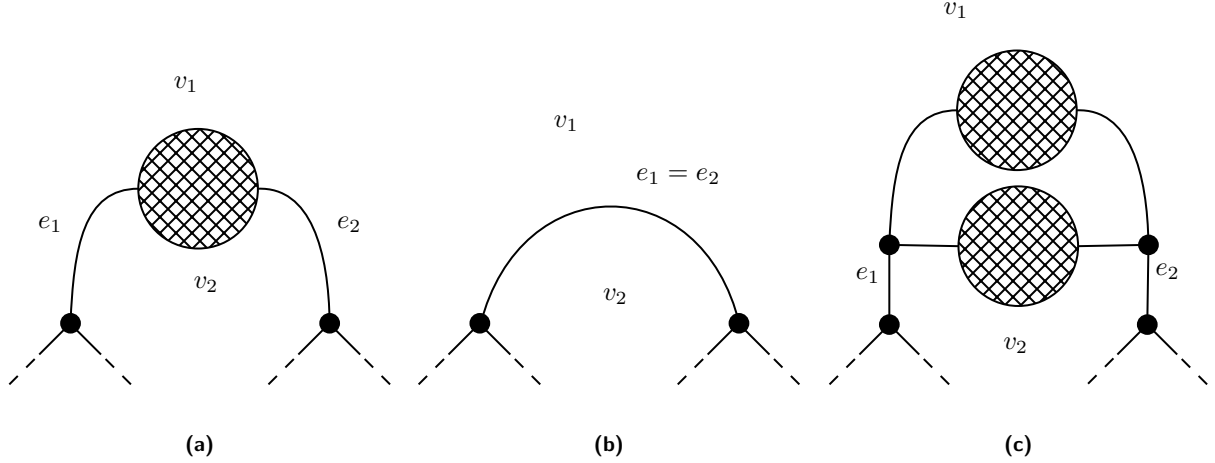


Figure D.3: The general case of two edges e_1, e_2 sharing their endpoints v_1, v_2 , represented as a dual graph, in (a). The crosshatched area denotes any ϕ^3 diagram with two legs. Figures (b) and (c) show the options for what this crosshatched area could be. The former shows the case where this shaded area is the simplest diagram with two legs: a single edge. In this case there is no two-neck. The latter shows the only other option when tadpoles are excluded: two self-energy diagrams in parallel.

To summarize, it has been shown that any triangulation in \mathcal{T}_{MD} can be transformed into one in \mathcal{T}_{RD} , and likewise any triangulation in \mathcal{T}_{RD} can be transformed into one in \mathcal{T}_C , in a finite number of edge flips. The edge flip is ergodic in \mathcal{T}_C , and thus the edge flip is also ergodic in both the degenerate ensembles.

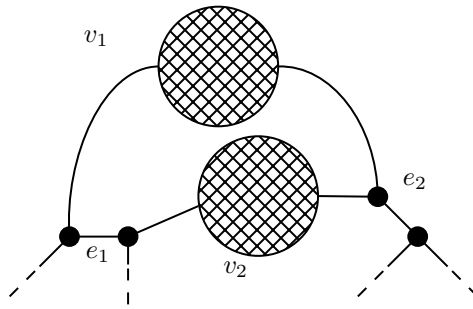


Figure D.4: The result of flipping edge e_1 of the self energy diagram of Figure D.3c.

Acknowledgements

I want to thank my supervisor, Renate, for providing supervision and guidance, and for the thorough proofreading of anything I would send in. I also want to thank Jesse van der Duin, Tom Gerstel and Agustín Silva, for all of our fruitful discussions. Finally, I want to thank Amy and my parents, for their patience and unwavering support throughout the process.

Bibliography

- [1] A. Einstein, “Die Grundlage der allgemeinen Relativitätstheorie,” *Annalen der Physik*, vol. 354, pp. 769–822, 1916. [Online]. Available: <https://onlinelibrary.wiley.com/doi/abs/10.1002/andp.19163540702>
- [2] The Event Horizon Telescope Collaboration *et al.*, “First M87 Event Horizon Telescope Results. I. The Shadow of the Supermassive Black Hole,” *Astrophys. J. Lett.*, vol. 875, p. L1, 2019.
- [3] A. Einstein, “Über Gravitationswellen,” *Sitzungsberichte der Königlich Preussischen Akademie der Wissenschaften*, pp. 154–167, 1918.
- [4] B. P. Abbott *et al.*, “Observation of gravitational waves from a binary black hole merger,” *Phys. Rev. Lett.*, vol. 116, p. 061102, 2016. [Online]. Available: <https://arxiv.org/abs/1602.03837>
- [5] N. Klitgaard and R. Loll, “Introducing quantum Ricci curvature,” *Physical Review D*, vol. 97, 2018. [Online]. Available: <https://arxiv.org/abs/1712.08847>
- [6] R. Loll, “Quantum Curvature as Key to the Quantum Universe,” in *Handbook of Quantum Gravity*, C. Bambi, L. Modesto, and I. Shapiro, Eds. Singapore: Springer Nature Singapore, 2023, pp. 1–35. [Online]. Available: https://doi.org/10.1007/978-981-19-3079-9_91-1
- [7] N. Klitgaard and R. Loll, “Implementing quantum Ricci curvature,” *Physical Review D*, vol. 97, 2018. [Online]. Available: <https://doi.org/10.1103/PhysRevD.97.106017>
- [8] J. Brunekreef and R. Loll, “Quantum flatness in two-dimensional quantum gravity,” *Physical Review D*, vol. 104, 2021. [Online]. Available: <https://arxiv.org/abs/2110.11100>
- [9] J. van der Duin, “Curvature correlations in quantum gravity: a numerical study of two-point functions in 2D CDT,” Master’s thesis, Radboud University Nijmegen, 2023. [Online]. Available: <https://www.ru.nl/highenergyphysics/theses/master-theses/>
- [10] H. Kawai, N. Kawamoto, T. Mogami, and Y. Watabiki, “Transfer matrix formalism for two-dimensional quantum gravity and fractal structures of space-time,” *Physics Letters B*, vol. 306, pp. 19–26, 1993. [Online]. Available: <https://arxiv.org/abs/hep-th/9302133>
- [11] J. Barkley and T. Budd, “Precision measurements of Hausdorff dimensions in two-dimensional quantum gravity,” *Classical and Quantum Gravity*, vol. 36, p. 244001, 2019. [Online]. Available: <https://arxiv.org/abs/1908.09469>
- [12] J. Ambjørn, J. L. Nielsen, J. Rolf, D. Boulatov, and Y. Watabiki, “The spectral dimension of 2D quantum gravity,” *Journal of High Energy Physics*, vol. 1998, pp. 010–010, 1998. [Online]. Available: <https://arxiv.org/abs/hep-th/9801099>
- [13] R. P. Feynman, “Space-time approach to non-relativistic quantum mechanics,” *Rev. Mod. Phys.*, vol. 20, pp. 367–387, 1948. [Online]. Available: <https://link.aps.org/doi/10.1103/RevModPhys.20.367>
- [14] R. Loll, G. Fabiano, D. Frattulillo, and F. Wagner, “Quantum Gravity in 30 Questions,” *PoS*, vol. CORFU2021, p. 316, 2022. [Online]. Available: <https://arxiv.org/abs/2206.06762>
- [15] C. Gattringer and C. B. Lang, *Quantum Chromodynamics on the Lattice: An Introductory Presentation*, ser. Lecture Notes in Physics. Berlin Heidelberg: Springer, 2010, vol. 788.

- [16] T. Regge, “General relativity without coordinates,” *Il Nuovo Cimento (1955-1965)*, vol. 19, pp. 558–571, 1961. [Online]. Available: <https://doi.org/10.1007/BF02733251>
- [17] R. R. Cuzinatto, C. A. M. de Melo, and C. N. de Souza, “Introduction to Regge calculus for gravitation,” 2019. [Online]. Available: <https://arxiv.org/abs/1904.01966>
- [18] J. Gallier and J. Quaintance, *Aspects of Convex Geometry: Polyhedra, Linear Programming, Shellings, Voronoi Diagrams, Delaunay Triangulations*. Philadelphia, PA 19104, USA: Department of Computer and Information Science, University of Pennsylvania, 2022, e-mail: jean@seas.upenn.edu.
- [19] J. Ambjørn, M. Carfora, and A. Marzuoli, *The Geometry of Dynamical Triangulations*, ser. Lecture Notes in Physics, New Series. Berlin: Springer, 1997, vol. 50. [Online]. Available: <https://arxiv.org/abs/hep-th/9612069>
- [20] G. Thorleifsson, “Three-dimensional simplicial gravity and degenerate triangulations,” *Nuclear Physics B*, vol. 538, pp. 278–294, 1999. [Online]. Available: <https://doi.org/10.1016%2Fs0550-3213%2898%2900679-8>
- [21] J. Ambjørn, “Elementary Quantum Geometry,” 2022. [Online]. Available: <https://arxiv.org/abs/2204.00859>
- [22] J.-F. L. Gall, “Random geometry on the sphere,” 2014. [Online]. Available: <https://arxiv.org/abs/1403.7943>
- [23] J. Distler and H. Kawai, “Conformal field theory and 2D quantum gravity,” *Nuclear Physics B*, vol. 321, pp. 509–527, 1989. [Online]. Available: <https://www.sciencedirect.com/science/article/pii/0550321389903544>
- [24] M. J. Bowick, S. M. Catterall, and G. Thorleifsson, “Minimal dynamical triangulations of random surfaces,” *Physics Letters B*, vol. 391, pp. 305–309, 1997. [Online]. Available: <https://www.sciencedirect.com/science/article/pii/S0370269396014591>
- [25] G. Miermont, “Aspects of random maps,” Saint-Flour lecture notes, 2014.
- [26] J. Ambjørn, G. Thorleifsson, and M. Wexler, “New critical phenomena in 2D quantum gravity,” *Nuclear Physics B*, vol. 439, pp. 187–204, 1995. [Online]. Available: <https://doi.org/10.1016%2F0550-3213%2895%2900014-j>
- [27] J. Ambjørn, J. Jurkiewicz, and Y. Watabiki, “On the fractal structure of two-dimensional quantum gravity,” *Nuclear Physics B*, vol. 454, pp. 313–342, 1995. [Online]. Available: <https://www.sciencedirect.com/science/article/pii/0550321395004688>
- [28] J. Brunekreef and R. Loll, “Curvature profiles for quantum gravity,” *Phys. Rev. D*, vol. 103, p. 026019, 2021.
- [29] T. Budd. (2023) Monte Carlo Techniques. Lecture notes for NWI-NM042B Monte Carlo Techniques, Radboud University, Nijmegen, The Netherlands. [Online]. Available: <https://hef.ru.nl/~tbudd/mct/mct.book.pdf>
- [30] D. Landau and K. Binder, *A Guide to Monte Carlo Simulations in Statistical Physics*, 5th ed. Cambridge University Press, 2021.
- [31] N. Metropolis, A. W. Rosenbluth, M. N. Rosenbluth, A. H. Teller, and E. Teller, “Equation of State Calculations by Fast Computing Machines,” *The Journal of Chemical Physics*, vol. 21, pp. 1087–1092, 1953.
- [32] W. K. Hastings, “Monte Carlo sampling methods using Markov chains and their applications,” *Biometrika*, vol. 57, pp. 97–109, 1970. [Online]. Available: <https://doi.org/10.1093/biomet/57.1.97>
- [33] D. Boulatov, V. Kazakov, I. Kostov, and A. Migdal, “Analytical and numerical study of a model of dynamically triangulated random surfaces,” *Nuclear Physics B*, vol. 275, pp. 641 – 686, 1986.

- [34] G. Peyré and M. Cuturi, “Computational Optimal Transport,” Center for Research in Economics and Statistics, Working Papers, 2017. [Online]. Available: <https://ideas.repec.org/p/crs/wpaper/2017-86.html>
- [35] S. Catterall, G. Thorleifsson, M. Bowick, and V. John, “Scaling and the fractal geometry of two-dimensional quantum gravity,” *Physics Letters B*, vol. 354, pp. 58–68, 1995. [Online]. Available: <https://doi.org/10.1016%2F0370-2693%2895%2900623-s>
- [36] A. A. Hagberg, D. A. Schult, and P. J. Swart, “Exploring network structure, dynamics, and function using networkx,” in *Proceedings of the 7th Python in Science Conference*, G. Varoquaux, T. Vaught, and J. Millman, Eds., Pasadena, CA USA, 2008, pp. 11 – 15.
- [37] C. R. Harris, K. J. Millman, S. J. van der Walt *et al.*, “Array programming with numpy,” *Nature*, vol. 585, pp. 357–362, 2020. [Online]. Available: <https://doi.org/10.1038/s41586-020-2649-2>